HHS Public Access

Author manuscript

Small. Author manuscript; available in PMC 2025 September 01.

Published in final edited form as:

Small. 2024 September ; 20(37): e2400815. doi:10.1002/smll.202400815.

Preformed vesicle approach to LNP manufacturing enhances retinal mRNA delivery

Yulia Eygeris[a,†], **Michael I. Henderson**[a,†], **Allison G. Curtis**[b], **Antony Jozic**[a], **Jonathan Stoddard**[c], **Rene Reynaga**[c], **Kathleen R. Chirco**[b], **Grace Li-Na Su**[b], **Martha Neuringer**[b,c], **Andreas K. Lauer**[b,c], **Renee C. Ryals**[b,#], **Gaurav Sahay**[a,b,d,*]

[a]Department of Pharmaceutical Sciences, College of Pharmacy, Oregon State University, Portland, Oregon 97201 USA

[b]Department of Ophthalmology, Casey Eye Institute, Oregon Health & Science University, Portland, Oregon 97201 USA

[c]Oregon National Primate Research Center, Oregon Health & Science University, Beaverton, OR 97006, USA

[d]Department of Biomedical Engineering, Oregon Health & Science University, Portland, Oregon 97201

Abstract

Complete encapsulation of nucleic acids by lipid-based nanoparticles (LNPs) is often thought to be one of the main prerequisites for successful nucleic acid delivery, as the lipid environment protects mRNA from degradation by external nucleases and assists in initiating delivery processes. However, delivery of mRNA via a preformed vesicle approach (PFV-LNPs) defies this precondition. Unlike traditional LNPs, PFV-LNPs are formed via a solvent-free mixing process, leading to a superficial mRNA localization as identified in cryoTEM imaging. While demonstrating low encapsulation efficiency in the RiboGreen assay, PFV-LNPs improved delivery of mRNA to the retina by up to 50% compared to the LNP analogs across several formulations containing benchmark ionizable lipids, suggesting the utility of this approach regardless of the lipid composition. Successful mRNA and gene editors' delivery was observed in the retinal pigment epithelium and photoreceptors and validated in mice, non-human primates, and human retinal organoids. This is the first report showing LNP-mediated transfection in the human retinal organoids. Deploying PFV-LNPs in gene editing experiments resulted in a similar extent of gene

[#]Corresponding author ryals@ohsu.edu. [*]Corresponding author sahay@ohsu.edu.
[†]Equal author contribution

Author contributions

Y.E., R.C.R., and G.S. conceptualized the study and research strategy. Y.E. performed formulation and characterization, cryoTEM acquisition, FFT analysis, in vivo imaging, writing, review, and revisions; M.I.H. performed formulation and characterization, cryoTEM acquisition, cell studies, *in vitro* and *in vivo* imaging, confocal imaging, and initial writing; R.C.R., A.C., and G.L.N.S. performed subretinal injections and image acquisition; A.C. and G.L.N.S. performed eye sections preparation, processing, and analysis; K.R.C. generated human retinal organoids, performed their transfection and IF imaging; J.S. and R.R. performed NHP IF sample preparation, image acquisition and analysis; A.J. performed intravenous injections; Y.E. and R.C.R. revised the manuscript with input from other authors; R.C.R., M.N. and A.K.L. directed retinal studies; G.S. directed research, writing, review, and funding acquisition.

Conflicts of Interest

G.S. is a co-founder of EnterX Bio and RNAvax Bio, and has an advisory role to Rare Air Inc. and Serina Tx. Y.E. has stock options and an advisory role to EnterX Bio. Other authors have no conflicts to declare.

editing compared to analogous LNP (up to 3% on genomic level) in the Ai9 reporter mouse model; but, remarkably, retinal tolerability was significantly improved for PFV-LNP treatment. The study findings indicate that the LNP formulation process can greatly influence mRNA transfection and gene editing outcomes, improving LNP treatment safety without sacrificing efficacy.

Keywords

Lipid nanoparticle; mRNA; gene delivery; retinal degeneration; IRD

Introduction

The eye is one of the high-priority targets for developing gene therapies to halt irreversible vision loss caused by ocular genetic diseases.[1] The posterior segment of the eye comprises the retina, with neuronal and epithelial cells essential for healthy vision. Currently, the subretinal route of administration allows for direct delivery of therapeutics to the retina. The FDA has approved only one treatment for inherited retinal disease, Luxturna (voretigene neparvovec-rzyl), which consists of an adeno-associated virus (AAV) subretinal treatment for Leber congenital amaurosis due to mutations in *RPE65*.[2] Non-viral carriers such as lipid nanoparticles (LNPs) have also achieved success in retina-oriented preclinical studies[3] and could be advantageous for delivery to the eye compared to AAVs as LNPs exhibit a low immunogenic profile, allow for repeated dosing, and do not possess cargo size limit.[4] Despite these successes, non-viral nucleic acid delivery to the eye remains in its infancy and there is a need for innovative approaches to the engineering of non-viral delivery systems.[5]

LNPs have been successfully employed for delivery of siRNA,[6,7] mRNA,[8–10] and gene editors,[11] aiming to treat and prevent a wide range of diseases. LNPs usually consist of an ionizable lipid, structural lipids, and a polymer-conjugated lipid (e.g., polyethylene glycol (PEG)-lipid). Typically, LNP formulation involves a method of rapidly mixing lipid and nucleic acid phases, followed by nanoprecipitation and growth of LNPs, removal of an organic solvent such as ethanol, and, finally, purification and concentration.[12] The tunability of lipid-nucleic acid interactions allows efficient cargo encapsulation and fine-tuning of the carrier properties either by adjusting the formulation or the manufacturing processes.[13–15] High encapsulation efficiency, arising from electrostatic interaction between nucleic acids and ionizable lipids, is universally thought to be a major requirement for the robust delivery of therapeutic cargo and for protecting the nucleic acid from degradation by the nucleases.

Previously, Kulkarni et al. reported solvent-free preparation of LNPs containing siRNA.[16] In contrast to a standard, single-step microfluidic mixing of lipid solution in ethanol with acidic siRNA solution to form LNPs, their method consisted of first generating empty lipoplexes (later termed preformed vesicles, or PFVs), removing the organic solvent by dialysis against acidic buffer, and then mixing the acidic PFV suspension with siRNA (the product of which is further termed PFV-LNPs). These siRNA PFV-LNPs were virtually indistinguishable from those made via standard two-phase mixing. This fascinating observation suggests that nucleic acid encapsulation occurs independently of nanoparticle

formation since nanoparticle formation and growth rely on hydrophobic forces[12]. However, a possible limitation to this hypothesis is the size of the nucleic acid, since siRNA typically consists of <100 nucleotides and may be able to diffuse into the LNP. Messenger RNA, on the other hand, typically comprises >1000 nucleotides and potentially has more accessible phosphate groups compared to siRNA due to its single-stranded nature. Therefore, we thought to investigate the application of this solvent-free process to mRNA delivery.

In this work, we investigated whether the solvent-free mixing approach applies to encapsulation of mRNA and gene editors in PFV-LNPs. We anticipated that this mixing process would lead to significant deviations in size, architecture, and lipid density at the lipid membrane-nucleic acid interface compared to conventional LNPs. We chose DLin-MC3-DMA, SM-102, ALC-0315, and LP01 ionizable lipids in their respective formulations for our studies since these ionizable lipids are currently used in LNP-based clinical products. We found that PFV-LNPs display a perceived drop in mRNA encapsulation efficiency which is the result of blebbed nanoparticle morphology and not poor mRNA loading as evident from cryoTEM imaging. Since the lipid core formation and electrostatic mRNA binding are separated into different steps, we anticipated that mRNA encapsulated in PFV-LNPs may be less stable due to the higher diffusion barrier for much longer mRNA chains to enter the lipid space. On the other hand, this could provide a faster release profile, beneficial for delivery in local targets. Indeed, we have found that the PFV-LNPs were unable to transfect organs from systemic administration as efficiently as their LNP counterpart; however, the blebbed PFV-LNP morphology has proven to be beneficial in subretinal administration in terms of improving transfection efficiency and retinal health. These findings bring to attention the importance of cargo packing for future non-viral retinal therapeutics.

Results and Discussion

Preformed vesicle and nanoparticle preparation and properties.

In this report, we utilize the following nomenclature: PFV – preformed vesicles, pure lipid-based vesicles without mRNA; PFV-LNPs – preformed vesicles loaded with mRNA; LNP – standard, two-phase (organic + aqueous) microfluidic mixing of lipid nanoparticles with mRNA. The formulation process for PFV-LNPs has more steps than a standard LNP manufacturing process, as illustrated in Figure 1A. Initial preformed lipid vesicles (PFVs) are prepared by microfluidic mixing at a 3:1 volumetric ratio of aqueous to organic solutions, respectively. The organic phase contained an ionizable lipid DLin-MC3-DMA (MC3), DSPC, cholesterol, and DMG-PEG-2000 (50:10:38.5:1.5 molar ratios) dissolved in pure ethanol, and an aqueous phase consisting of 50mM citrate buffer (pH 4). To remove the solvent post-mixing, PFVs were dialyzed against citrate buffer for 24 hours. Then, PFVs underwent a second, single-phase microfluidic mixing at a 3:1 volumetric ratio between aqueous PFV and mRNA solutions to yield PFV-LNPs. Subsequently, PFV-LNPs were dialyzed against phosphate buffer saline (PBS, pH 7.4). LNPs were prepared via a standard protocol where the aqueous phase included mRNA (Figure 1A; from step 1 directly to step 4); these nanoparticles were used as a formulation control. Depending on the experiment, the mRNA encoded either Firefly luciferase (FLuc), Cre recombinase (Cre), or enhanced green fluorescent protein (EGFP).

Characterization of hydrodynamic sizes by dynamic light scattering (DLS) revealed that LNPs and PFVs possessed similar diameter and size distribution (ca. 100 nm) while the PFV-LNPs nearly doubled in size regardless of the cargo (Fig. 1B and S1A). The polydispersity index (PDI) did not change significantly and the LNP population remained fairly monodisperse (PDI < 0.2; Fig. S1A). Unloaded PFVs had a true neutral surface charge, as indicated by zeta potential (ZP) of ca. 0 mV (Fig. 1C). Among traditional LNPs, Cre LNP had a stronger surface charge (ZP ca. −15 mV) while FLuc and EGFP LNPs had ZP < −5mV. When these mRNAs were incorporated in PFV-LNPs, the surface charge was strongly dependent on the mRNA. Fluc PFV-LNP became significantly more negative (ZP ca. −15 mV), EGFP PFV-LNP remained roughly the same, and Cre PFV-LNPs had a reduced negative charge (ZP ca. −10mV). This change in ZP could be a result of sequence-specific packing of mRNA inside LNPs and adhesion or penetration of the lipid surface, e.g. due to the secondary structure of mRNA sequences.[17] The hypothesis of superficial mRNA localization is supported by the results of a modified RiboGreen encapsulation efficiency assay, as PFV-LNPs internalized ca. 50% of RNA while LNPs yielded nearly complete mRNA encapsulation (Fig. 1D). The mRNA in PFV-LNPs was also highly susceptible to enzymatic degradation as demonstrated by the RNAse protection assay (Fig. S1B), suggesting that mRNA is not sufficiently shielded by the lipid environment in PFV-LNP nanoparticle format. This may indicate an inferior stability of the PFV-LNPs, since lipid-based nanocarriers tend to protect mRNA from degradation in this assay.[18,19]

mRNA localization may be associated with lipid membrane reorganization; therefore, we employed a Laurdan assay to determine the differences in lipid membrane hydration and packing (Fig. 1E).[20–22] Laurdan is a hydrophobic fluorescent dye commonly used to investigate cellular membrane properties and microscale packing, and this assay was previously used to characterize the changes in lipid membrane hydration in response to pH for siRNA and mRNA LNPs.[21,22] As the pH becomes more acidic, ionizable lipids acquire a positive charge and solvate with water, which causes a decrease in generalized polarization (GP) and indicates looser packing of the lipid bilayer or higher water content. MC3 LNPs possess pKa of ca. 6.4,[23] and, indeed, we observe a characteristic GP drop at pH < 6.5 from 0.4 to 0.2. PFVs demonstrated overall lower GP compared to LNPs, and the magnitude of pH response was identical to LNPs. This could be the result of a larger quantity of available cationic groups in the absence of mRNA. PFV-LNP samples, however, had a much smaller magnitude of GP change with pH and had the highest GP values in the series, suggesting the tightest lipid membrane packing in the series.

Cryo-TEM micrographs of PFV-LNPs revealed a distinctive morphology containing superficial electron-dense pockets of mRNA (Fig. 1F), which explains the results of the RiboGreen assay and ZP measurements. The controlled manufacturing of blebbed mRNA nanostructures is not common but can be achieved by introducing lipids that may change the overall hydrophobicity of the nanoparticle[24] or by manipulating the ionic strength of the acidic buffer.[25] LNPs, on the other hand, were generally uniform and amorphous, and PFVs produced a range of lipid structures – homogenous, onion-like, and other organized structures that did not persist after mRNA was introduced. Furthermore, unlike PFV-LNPs, PFVs produced some highly ordered structures at pH 4. To investigate the potential crystal structure of PFVs, we performed high-resolution TEM (HRTEM) image analysis.

The micrographs revealed lamellar and hexagonal packing with approximate d-spacing of ca. 2.5 and ca. 5.2 nm, respectively (Fig. S2). The formation of lamellar structures is frequently observed for LNPs;[24,26] yet, there are limited reports capturing the properties of the hexagonal phase in LNPs.[27–29] The formation of an inverse hexagonal phase is thought to correlate with fusogenicity with intracellular membranes.[30,31] The formation of the hexagonal phase has been previously observed only in the presence of mRNA and ascribed to the encapsulation of mRNA into stacked aqueous channels at both acidic and neutral pH,[27] but our results indicate that the formation of the hexagonal phase may be characteristic of the lipids, independently of the nucleic acid. Since mRNA is localized superficially in PFV-LNPs, the core of PFV-LNPs is likely only affected by the pH. The PFVs then rearranged upon pH neutralization and lost the hexagonal structure in favor of lamellae upon pH neutralization (Fig. 1F), similar to other reports.[27–29]

Considering the increased negative charge and superficial localization of mRNA pockets, observation of tight lipid membrane packing seems counterintuitive but plausible if the lipid components reorganize – e.g., shuttling of ionizable lipid to lipid-mRNA interface from the exterior lipid membranes. A similar observation of lipid reorganization (although upon exposure to protein) has been reported by Sebastiani and colleagues.[32] Indirect evidence of the lipid reorganization is a potential thinning of the outermost lamellae (ca. 2.5 nm compared to the ca. 3 nm we have previously reported for LNPs[24]).

In vitro transfection and endosomal escape assessment.

Next, we evaluated the transfection and endosomal escape capabilities of PFV-LNPs containing FLuc mRNA. Our group previously observed that LNP morphology can influence transfection and endosomal trafficking,[21,24,33,34] and so we were curious to see how PFV-LNP could affect transfection. Four cell lines – HeLa (human cervical epithelial cell line), ARPE19 (human retinal pigmented epithelial cells), 661w (murine photoreceptors), and Gal9-GFP HEK293T/17 (human embryonic kidney cell line engineered to produce GFP-fused galectin 9 to visualize endosomal escape[21,35]) – were dosed with PFV-LNPs and LNPs and assayed after 24 hours. The dose was calculated as the total mRNA concentration regardless of the encapsulation efficiency to avoid the discrepancies from the reduced encapsulation efficiency of PFV-LNPs. Cell viability was maintained at >95% for all treatment groups, suggesting that there are no adverse effects due to the PFV-LNP structure (Fig. S3). Transfection ability appeared cell-specific, as PFV-LNPs produced 2-fold more efficient transfection in HeLa cells compared to standard LNP, whereas ARPE19 yielded no statistically significant differences and 661w yielded 2-fold lower transfection efficiency for PFV-LNPs compared to LNPs (Figure S3). Imaged-based analysis of Gal9 recruitment after 200 ng mRNA treatment for 24 hours showed a 2-fold increase for PFV-LNPs compared to LNPs (Fig. 1G). The results for 50 ng treatment, however, were not significantly different, which may be due to the limitations of assay sensitivity (higher doses may result in a greater number of particles present and a higher degree of cellular uptake).

Intravenous mRNA delivery.

Encouraged by *in vitro* results, we sought to investigate the potential differences between LNP and PFV-LNP *in vivo*. First, we evaluated transfection differences upon intravenous administration to mice, anticipating that the superficial localization of mRNA PFV-LNPs may compromise the particles' ability to sustain efficient delivery upon exposure to the bloodstream due to the aggregation with serum proteins. We administered 1.5 μg of FLuc mRNA in either LNPs or PFV-LNPs to Balb/c mice intravenously and monitored transfection efficiency by bioluminescent imaging. As mentioned above, the dose administered was calculated based on the total mRNA concentration found in the LNP or PFV-LNP samples, since the RiboGreen assay cannot differentiate between unbound and superficially localized or protruding mRNA. Indeed, we found that the transfection efficiency of PFV-LNPs was unremarkable – almost 2 orders of magnitude lower than that of LNPs at both 4 and 24-hour time points (Figure S4). The pattern of bioluminescence in all cases was indicative of liver transfection, typical for LNPs.[23] The heterogeneity of PFV-LNPs likely triggered premature nucleic acid release from the aqueous pockets and compromised their ability to deliver mRNA. Notably, our findings do not agree with the recent report by Cheng et al.[25] suggesting that blebbed LNP architecture is beneficial for intravenous mRNA delivery; however, their approach to blebbed LNP manufacturing involved varying the ionic strength of the solution and not the order of mixing steps, which may have entirely different consequences on the lipid packing and mRNA release.

mRNA delivery to the murine retina via subretinal injection.

After observing the decrease in transfection after systemic delivery, we hypothesized that the superficial mRNA localization may lead to the rapid release of mRNA from the PFV-LNP structure, which could be beneficial in local administration. To evaluate this hypothesis, we have chosen the subretinal route of administration. Previously, our group investigated the delivery of mRNA via LNPs to the retina and found that MC3 formulation successfully delivered mRNA to retinal pigment epithelium (RPE) and Müller glia.[36,37] We expected to see similar cell specificity for MC3 PFV-LNPs. We used Cre recombinase-encoding mRNA in Ai9 mice experiments to evaluate cell specificity, and EGFP-encoding mRNA in 129X1/SvJ mice experiments to measure the extent of protein expression.

Successful delivery of Cre recombinase in the Ai9 mouse model leads to the expression of tdTomato, which is a useful screening tool to evaluate cell specificity in various organs (Figure 2A).[38] At 1 week post-subretinal administration of 400 ng Cre mRNA, both LNPs and PFV-LNPs induced tdTomato signal in mouse retina at significant levels compared to PBS control (Fig. 2B). Immunofluorescence (IF) of tissue sections showed that tdTomato+ signal was absent in retina sections of PBS-treated mice, while both LNP and PFV-LNP groups showed prominent transfection of retinal tissues (Fig. 2C). Notably, PFV-LNP treatment produced a more uniform tdTomato expression across the bleb, indicating a better spread through the retinal tissue compared to standard LNP. Both treatments transduced RPE, Müller glia, and few photoreceptors, but all were more pronounced in the case of PFV-LNP. While the mean tdTomato pixel signal intensity in RPE and outer nuclear layer (ONL) was 2–3 times higher in PFV-LNP group than LNP, the differences were not statistically significant (Fig. S5). This was expected as the tdTomato cassette is under

a strong ubiquitous promotor and thus the amount of Cre recombinase delivered is not proportional to the protein expression. No acute retinal toxicity (i.e., uveitis) was observed in fundus images; however, ONL and INL were more disrupted in the LNP-treated retina, suggesting that PFV-LNPs may have better retinal tolerability.

To quantify the extent of mRNA transfection efficiency and protein expression, we administered LNP and PFV-LNPs carrying EGFP mRNA subretinally to 129X1/SvJ mice. Fundoscopy at 48 hours post-injection of 200 ng EGFP mRNA revealed stronger GFP signal for the PFV-LNP group (Fig. 3A). Only RPE had a strong GFP-positive signal in the eye sections from both treatment groups, with more pronounced transfection for PFV-LNP group (Fig. 3B). Quantification of the GFP signal in fundus and IF images confirmed higher transfection by PFV-LNPs (Fig. 3C), with ca. 50% higher GFP signal in fundus images and ca. 20% higher in IF. The discrepancy is the result of autofluorescence in the fundus images. The “wispy” pattern seen in some sections of ONL revealed that PFV-LNP treatment reached photoreceptors, although in a small area (Fig. 3D). The increased retinal transfection efficiency observed with PFV-LNPs is remarkable, since it was achieved by a simple modification of the manufacturing process. Expression of target proteins both in the case of Cre and EGFP mRNA in RPE was consistent and expected due to the phagocytic nature of RPE. The discrepancies between cell specificity for Cre and EGFP mRNA nanoparticles are most likely due to the sensitivity of the Cre recombinase system, where very little Cre protein is needed to mediate robust levels of tdTomato. Additionally, this could be the result of the nanoscale changes in particle packing and other properties – for example, Cre nanoparticles were consistently more negatively charged than EGFP ones (Figure 1C), which we have shown to be desirable for efficient delivery to the photoreceptors.[39]

Intrigued by these results, we decided to investigate whether the potency and cellular targeting of PFV-LNPs in the retina is unique to MC3 formulations or if it could be extended to other lipids. For that, we compared PFV-LNP and LNPs containing two other potent ionizable lipids – SM-102 and ALC-0315, known for their use in COVID-19 vaccines. These ionizable lipids were incorporated in place of DLin-MC3-DMA with the same nanoparticle composition and formulation processes. The nanoparticles (both LNP and PFV-LNP) were formulated to include EGFP mRNA and administered to 129X1/SvJ mice. Indeed, we found that changing the manufacturing process enhanced retinal delivery. Again, the increase in EGFP signal was observed both in fundus and immunofluorescence images. The improvement in EGFP transfection for PFV-LNPs was consistent and significant (ca. 30–50% higher on average; Fig. 3C), suggesting that the PFV-LNP approach leads to an improvement in mRNA transfection in the back of the eye.

mRNA delivery via subretinal injection of PFV-LNP in non-human primate.

Although mouse models are frequently used in the studies of inherited retinal disease, they are a poor indication for potential translation to humans due to the smaller size of the eye, large lens, and absence of macula, among other factors.[40,41] Therefore, we evaluated whether MC3 PFV-LNPs, our ballpark formulation, retain the ability to transfect the retina and the photoreceptors in non-human primates (NHP).

25 μg of EGFP mRNA in PFV-LNP was administered to a rhesus macaque (N = 1 eye) via subretinal injection. Fundus autofluorescence imaging of the retina 48 hours post-injection revealed a clear GFP signal (Fig. 4A). Optical coherence tomography (OCT) revealed retinal detachment (Fig. 4H), likely persisting from the subretinal injection procedure which involves creating a detachment of the photoreceptor layers from the RPE – similar detachment was also observed in the control saline injections (Fig. S6). Some accumulation of debris was noted in the subretinal space, but it is not clear whether this is the result of toxicity, accumulation of LNPs, or the mechanical stress of the injection. Staining the retina sections with cone arrestin, RPE65, and anti-GFP antibodies revealed good colocalization with GFP expression, confirming successful transfection of photoreceptors and RPE (Fig. 4B–G). We deployed an image-based quantification approach and estimated that 29% of cones, 10% of rods, and 66% of RPE cells were EGFP-positive. Transfection was uniform across the treated bleb (Fig. 4I). IF imaging of CD3 and IBA1 -stained sections suggests some infiltration of the retina with T-cells and activated microglia/macrophages (Fig. 4J–L). This may indicate the need to reduce the dose or modify the treatment protocol to include an immunosuppressant treatment to negate the immune response to exogenous mRNA.[42] While we cannot draw a direct comparison between LNP and PFV-LNP in this experiment, GFP expression in photoreceptors was 1) markedly more pronounced in NHP than in mice, emphasizing the species-dependent differences in transfection efficiency and 2) lower in rods than in our previous study evaluating the subretinal delivery of mRNA with Thio-lipids (33% of rods at equivalent dose).[42]

mRNA delivery in human retinal organoids.

Retinal organoids generated from induced pluripotent stem cells (iPSCs) offer an insight into human retina development and may be used in the discovery of new retinal therapies.[43] These cells spontaneously self-organize in three-dimensional cell culture and develop structures naturally present in the eye, including an ONL with rod and cone photoreceptors, and, sometimes, a cluster of retinal pigment epithelium. We evaluated the transfection of patient-derived retinal organoids with EGFP PFV-LNPs to investigate the translational potential of the PFV-LNP treatment. To do so, we administered EGFP mRNA via MC3 PFV-LNPs to mature (D200–400) retinal organoids (Fig. 5A).[44] EGFP signal, which is indicative of successful transfection and mRNA expression, was observed in the photoreceptor (PR) layer after dosing the organoids with 2μg EGFP mRNA (Fig. 5B). Notably, both LNPs and PFV-LNPs could transfect the RPE layer of retinal organoids with high efficiency (Fig. 5C) after 10μg EGFP mRNA treatment, although we could not draw quantitative comparison of transfection efficiency in this system under the tested conditions. To a small extent, cone photoreceptors could also be transfected with PFV-LNPs (Fig. 5D). No clear dose response emerged upon treating the retinal organoids with up to 15μg of EGFP-mRNA in PFV-LNPs (Fig. S7A). Overall, these findings allude to PFV-LNP having the potential for efficient delivery in human patients, especially for the treatment of retinal degenerative diseases where RPE is implicated.

PFV-mediated subretinal delivery of gene editors.

Lastly, we evaluated whether the PFV-LNP manufacturing process is compatible with the delivery of gene editors. To do so, we prepared LNPs and PFV-LNPs containing ionizable

lipid LP01 and 1:1 wt/wt Cas9 mRNA and sgRNA targeting the loxP stop codon in Ai9 mice (sgAi9).[39] Lipid LP01 is engineered to deliver the gene editing systems with high efficiency and is currently evaluated in the clinics as a part of the NTLA-2001 gene editing treatment. We also prepared PFV-LNPs containing the non-targeting sgRNA (sgGFP) in place of sgAi9 as a negative control. The formulation composition and purification process were the same as reported originally for LP01 LNPs.[45] Unlike previous experiments, LP01 lipid was more efficient at capturing and absorbing nucleic acids, leading to 98% encapsulation efficiency, the same as for standard LNP (Figure 6A). LP01 LNPs were also slightly larger than PFV-LNPs (ca. 120 nm vs ca. 90 nm for PFV-LNPs) and less negatively charged (ca. −9 mV vs −15 mV for PFV-LNPs). 200 ng of total nucleic acid was administered subretinally to Ai9 mice, and their eyes were harvested 7 days after injection. Since we anticipated the majority of the editing events to occur in RPE based on the mRNA experiments, the eyes were processed into RPE flatmounts according to a previously published protocol.[46] The extent of gene editing and the amount of intact RPE cells was then quantified through image-based analysis of treated bleb and whole flatmounts. We have found that there was an increased fraction of transfected RPE (ca. 20% for LNP vs 37% for PFV-LNP within the treated areas) (Figures 6B,C); however, the extent of editing found by the next-generation sequencing (NGS) was very similar between treatments (approx. 3% in RPE) (Figure 6E). Unexpectedly, there was a higher amount of intact RPE cells present, which indicates a better tolerability of PFV-LNP treatment compared to LNP (ca. 94% vs 85%, respectively, of total RPE after sgAi9 treatment and ca. 90% vs 81% for sgGFP treatment; data shown in Figure 6D). This change is remarkable, suggesting that a simple reorganization of LNP components may benefit the safety profile of LNP-based ophthalmic therapies.

Discussion

Despite numerous efforts dedicated to the improvement of lipid chemistry[47] or formulations,[14] LNP architecture is not a topic that is often raised in the discussion of transfection potential. However, it is increasingly clear that upstream and downstream LNP formulation processes (i.e., adjustment of buffers and excipients[21,25,48,49]) may influence transfection efficiency. Harnessing the power of self-assembly to rearrange the lipid components into a more potent structure may provide an opportunity to engineer potent LNPs without navigating the vast chemical space of lipid structures.[50]

Controlled and reproducible manufacturing of nucleic acid-encapsulating nanoparticles has become a routine practice through the ubiquitous use of rapid mixing approaches like microfluidics. Homogenous (core-shell) and lamellar morphologies are the most commonly observed architectures of LNP, although cubic morphologies can also be manufactured.[50] Heterogeneous structures, on the other hand, are typically seen as undesired byproducts since they may be indicative of the aggregation and imminent loss of mRNA.[51] However, enhanced mRNA transfection by heterogeneous blebbed LNPs in vitro[24] and in vivo[25] contradicts this narrative.

In a normal LNP evaluation process, blebbed structures like the PFV-LNPs would fail a quality control check since they possessed a remarkably low encapsulation efficiency (ca. 50% as determined by the RiboGreen assay) despite containing a significant amount of

mRNA. The superficial mRNA localization comes at the high price of being susceptible to enzymatic degradation, which renders them significantly less active upon intravenous administration. This is a stark contrast to the report by Cheng et al., where blebbed LNPs had >90% encapsulation efficiency, enhanced in vivo transfection, and preserved mRNA integrity even after 24h incubation in serum.[25] However, to generate the blebbed LNPs, they used an elevated acidic buffer concentration (300 mM), which may cause reorganization of the lipids throughout the particle. We speculate that while these blebbed LNPs may appear similar, the lipid membrane interface may possess dramatically different lipid packing and contain different lipid composition, which could impede the penetration of the RiboGreen dye. For example, our Laurdan assay data suggests that PFV-LNPs have significantly less water content at the surface compared to their LNP counterpart, which could make the resulting lipid nanomaterials more “brittle” in aqueous suspensions. With the help of cryoTEM, we were able to capture how the fine structure of PFVs evolves from hexagonal at pH 4 (Fig. S2) to somewhat lamellar at pH 7.4 (Fig. 1F). The lamellar architecture in the lipid core is lost upon incorporation of mRNA in favor of bleb formation in PFV-LNPs (Fig. 1F), once again suggesting lipid reorganization at the nanoparticle interface.

While PFV-LNPs may be susceptible to enzymatic degradation, they performed well in the back of the eye where exposure to the RNAses, typically abundant in blood plasma, is not a major concern. PFV-LNPs improved EGFP mRNA transfection in mouse retina by up to 50% in DLin-MC3-DMA, SM-102, and ALC-0315 formulations compared to LNP. When administered to the NHP retina, we observed high transfection efficiency in RPE (66%) and lower transfection in photoreceptors (29% of cones and 10% of rods). Preference for RPE was maintained in the human retinal organoid culture experiments. Although we could not compare transfection efficiency between LNP and PFV-LNP in a quantitative manner in NHP and retinal organoids, PFV-LNPs overall had a more favorable toxicity profile compared to our previous findings in non-human primates; however, the transfection efficiency in photoreceptors was lower compared to Thio-lipids established in our lab.[42] PFV-LNP treatment presented similar RPE gene editing efficacy, but a better tolerability profile compared to LNP. We acknowledge that more work is needed to compare transfection efficiency and long-term tolerability between LNP and PFV-LNP in both NHP and retinal organoid models in a quantitative manner. Overall, PFV-LNPs present as a facile, easy to implement approach to improve tolerability of retinal treatments where RPE is the cellular target. This is critical, since human retinal cells do not regenerate and any treatment-associated damage may outweigh the potential benefits for retinal therapies and have lasting consequences on vision. Although it is not entirely clear what yields this advantage, we offer a following hypothesis. Since the number of electrostatic interactions between the lipids and the mRNA is more limited in the PFV approach than in the standard LNPs due to the available surface area, there is a lower probability of formation of lipid-mRNA adducts that can introduce unintended impurities and compromise translational competency of mRNA.[52]

Conclusion

In this report, we investigated whether “wrapping” a preformed lipid nanoparticle core with mRNA in a single-phase mixing process offers an advantage compared to traditional LNPs in cell and animal models. The PFV-LNP approach described herein appears to produce

a sustained benefit in local administration to the back of the eye, especially in terms of treatment tolerability. The extension of this approach to other local delivery routes, including vaccine applications, would be an interesting future direction. The PFV approach may have a tremendous utility in the LNP discovery pipeline, where a large batch of PFVs could be split, mixed with a small quantity of various genetic cargos, and evaluated in a respective target or application. Our findings present a strong case for considering the nanoparticle assembly process and resulting architecture in the development of gene therapies.

Materials and Methods

Materials

Ionizable aminolipid [(6Z,9Z,28Z,31Z)-heptatriaconta-6,9,28,31-tetraen-19-yl] 4-(dimethylamino) butanoate (DLin-MC3-DMA) was custom synthesized by BioFine International (Blaine, WA). Ionizable aminolipids SM-102 (9-heptadecanyl 8-{(2-hydroxyethyl)[6-oxo-6-(undecyloxy)hexyl]amino}octanoate) and ALC-0315 ([(4-hydroxybutyl)azanediyl]di(hexane-6,1-diyl) bis(2-hexyldecanoate)) were purchased from BroadPharm (San Diego, CA). 1,2-distearoyl-sn-glycero-3-phosphocholine (DSPC) was purchased from Avanti Polar Lipids, Inc (Alabaster, AL). CleanCap Firefly luciferase (L-7202), EGFP (L-7201), Cre (L-7211) and Cas9 (L-7606) mRNA were purchased from TriLink Biotechnologies. All preformed vesicles and lipid nanoparticles were prepared using Nanoassemblr Benchtop microfluidic mixer (Precision Nanosystems, Vancouver, BC). Nanoparticle characterization for size, polydispersity, and zeta potential was performed on Malvern Zetasizer ZS (Malvern Panalytical Inc., Westborough MA). Paraformaldehyde and lacey carbon grids for cryo-TEM imaging were purchased from Electron Microscopy Sciences (Hatfield, PA). Millipore Sigma Amicon® ultracentrifugal concentrators, cholesterol, and 1,2-dimyristoyl-rac-glycero-3-methoxy polyethylene glycol-2000 (DMG-PEG_{2k}) were purchased from Millipore Sigma (Millipore Sigma, Burlington, MA). Laurdan dye, sodium citrate dihydrate, citric acid, sodium hydroxide, phosphate buffer saline, ethanol, and Slide-A-Lyzer™ G2 dialysis cassettes, Quant-it™ RiboGreen RNA reagent, CellTiter-Fluor™ Cell Viability and ONE-Glo™ Luciferase assay kits, and all cell culture reagents were purchased from ThermoFisher Scientific (Federal Way, WA). Triton™ X-100 was purchased from Acros Organics. Fluorescence was acquired using a Tecan Infinite M200 Pro multimode microplate reader (Tecan Trading AG, Switzerland).

Animals

All mouse experiments were completed at Oregon Health & Science University and abided by the Institutional Animal Care and Use Committee (IACUC: TR01_IP00001707 and TR02_IP00000610) and the Association for Research in Vision and Ophthalmology (ARVO) Statement for the Use of Animals in Ophthalmic and Vision Research. Albino BALB/c (Cat#000651), Ai9 (Cat#007909), 129X1 (Cat#000691) mice were either bred in-house or purchased from The Jackson Laboratory (Bar Harbor, ME, USA). Ai9 mouse model is a Cre reporter tool designed with a loxP-flanked STOP cassette restricting transcription of red fluorescent (tdTomato) protein. Cre-mediated recombination in Ai9 mice leads to the expression of tdTomato. SVJ-129 (Cat# 002448) were used for eGFP expression experiments. Both male and female mice aged 1 to 5 months were used in experiments.

One adult rhesus macaque was involved in this study (aged 10 years old). All protocols involving NHPs were approved by OHSU IACUC (Protocol TR02_IP00000768) and were in adherence to the Institutional Biosafety Committee at the Oregon National Primate Research Center. The macaque was cared for daily, and all experimental procedures abided by the Association for Research in Vision and Ophthalmology (ARVO) Statement for the Use of Animals in Ophthalmic and Vision Research. All guidelines outlined in the National Institutes of Health Guide for the Care and Use of Laboratory Animals were rigorously followed.

Preformed vesicle and nanoparticle formulation and characterization

All formulations were generated through microfluidic mixing using the Nanoassemblr Benchtop mixer. Two phases were used to prepare either standard LNPs or PFVs. The organic phase contained an ionizable lipid, DSPC, Cholesterol, and DMG-PEG-2000 in ethanol at 50:10:38.5:1.5 molar ratio and total lipid concentration of 5.5 mM, and the aqueous phase contained 50 mM sodium citrate buffer (pH 4) with RNA (for LNP) or without RNA (for PFV). The ethanol phase containing all lipids dissolved was rapidly mixed with aqueous phase at 1:3 volumetric ratio, respectively, at 9 mL/min total flow rate. Following microfluidic mixing, the resulting suspension was immediately transferred to 10 kDa molecular weight cut-off (MWCO) cassettes and dialyzed against at least 300-fold volume of buffer overnight. For LNPs, the buffer used was 1x PBS; for PFVs, the buffer was pH 4 50mM sodium citrate. Following dialysis, the particles were concentrated using Amicon® Ultra centrifugal filter units with a 10 kDa MWCO at 3000g.

To prepare PFV-LNPs, RNA solution was prepared at identical volumes as for an equivalent batch of LNPs, and PFVs were diluted with citrate buffer to achieve 3:1 volumetric ratio between RNA:PFV mixtures. For gene editing experiments, 1:1 wt/wt Cas9 mRNA:sgRNA were added to pH 4.5 50mM acetate buffer. Two guide RNAs were used with the following sequences: 1) sgAi9 (sgRNA targeting loxP cassette in Ai9 mice): AAGUAAAACCUCUACAAAUG; 2) sgGFP (non-targeting sgRNA): CUCGUGACCACCCUGACCUA. Similarly, two solutions underwent secondary microfluidic mixing at 9 ml/min, the resulting suspension was purified by dialysis against PBS overnight and collected as described above.

Nanoparticles were characterized for hydrodynamic size, polydispersity index, and surface zeta potential with a Zetasizer Nano ZS (Malvern Panalytical Inc., Westborough, MA). For Zetasizer analysis, nanoparticles were diluted 200-fold in PBS and triplicate measurements were obtained. mRNA encapsulation efficiency and concentration were quantified utilizing a modified Quant-it™ RiboGreen RNA (Invitrogen, Waltham, MA) protocol and a multimode microplate reader (Tecan Trading AG, Switzerland). The dose was calculated using the total concentration of mRNA found in samples. For RNAse degradation assay, RNase A was added to the samples before conducting the RiboGreen assay.

Membrane fluidity (Laurdan) assay

A Laurdan hydration assay was performed as described previously.[21] Laurdan dye was diluted to 100 μM in dimethylformamide (DMF). Citrate and phosphate buffers were titrated

to achieve the desired pH and prewarmed at 37°C for 15 minutes before use. Nanoparticle solutions were diluted to reach a final lipid concentration of 50 μM (estimated from mRNA concentration and assuming w/w lipid-mRNA ratio of 20). Samples were thoroughly mixed with buffers and Laurdan in a black 96-well plate and incubated for 30 minutes at room temperature in the absence of light. Generalized polarization (GP) enables measurement of the differences in emission shift from a (gel) packed phase (440 nm) to a (liquid) disordered phase (490 nm). The GP was calculated as

$$GP = (I_{440} - I_{490})/(I_{440} + I_{490}),$$

where I – intensity at respective wavelengths. Each assay contained three technical replicates.

Cryo-electron microscopy and Fast Fourier Transform analysis

Cryo-transmission electron microscopy (cryo-TEM) was performed at 200kV using FEI Titan Glacios equipped with a Gatan K3 camera. 2–3 μL of nanoparticle sample was deposited on a plasma-cleaned grid (lacey carbon, 300 Cu mesh; plasma cleaning at 15 mA for 60 seconds using a Pelco EasiGlow 91000 Glow Discharge Cleaning System). After 10s rest time at 85–100% relative humidity, grids were blotted for 1 second and rapidly plunged into liquid ethane. The frozen grids were then checked for visible defects, assembled into cassettes under liquid nitrogen, and imaged. Sample images were acquired at −2.5 micron target defocus height. Crystallinity and lamellarity of PFV samples were assessed by extracting the ROI from high magnification images and applying Fast Fourier Transform (FFT) to uncompressed, unmodified images in ImageJ/Fiji.

Cell culture and *in vitro* transfection

HeLa, Gal9-GFP HEK293T/17 and ARPE19 cell lines were obtained from ATCC (Manassas, VA) and 661W cell line were a kind gift from Dr. Muayyad Al-Ubaidi (University of Oklahoma Health Sciences Center, Oklahoma City, OK). HeLa and Gal9-GFP HEK293T/17 cells were cultured in Dulbecco's modified Eagle's medium supplemented with 10% heat-inactivated fetal bovine serum (Hyclone Laboratories Inc., Logan, UT) and 1% penicillin/streptomycin (Thermo Fisher, Federal Way, WA). ARPE19 cells were cultured in Dulbecco's Modified Eagle Medium/Nutrient Mixture F-12 supplemented with 10% heat-inactivated fetal bovine serum and 40 μg/ml gentamicin (Thermo Fisher, Federal Way, WA). 661W cells were cultured in Dulbecco's modified Eagle's medium supplemented with 10% heat-inactivated fetal bovine serum, 40 μg/L hydrocortisone, 40 μg/L progesterone, 32 μg/L putrescine, 1% penicillin/streptomycin, and 40 μL/L beta-mercaptoethanol (Thermo Fisher, Federal Way, WA). All cultures were grown in 37°C incubators with a maintained 5% CO_2 according to suppliers' instructions.

For *in vitro* transfection studies, HeLa cells were plated at 4,000 cells per well, and ARPE19 and 661W cells were plated at 50,000 cells per well in 96-well plates and allowed to adhere overnight. Then, lipid nanoparticles encapsulating firefly luciferase mRNA were diluted with PBS to the appropriate concentration and added to the cells. To measure cell viability and luciferase expression, CellTiter-Fluor™ and ONE-Glo™ Luciferase assays were used

(Promega, Madison, WI). Fluorescence and luminescence measurements, respectively, were taken at 24 hours post-treatment with a microplate reader. Cell viability was determined by dividing the fluorescent signal of treated cells by the signal in PBS-treated cells. The luminescent signal (relative luminescence units, RLU) was normalized by the fluorescent signal (relative fluorescence units, RFU) to yield normalized transfection efficiency.

Visualization of Gal9-GFP recruitment in HEK293T/17 cells

HEK293T/17 Gal9-GFP reporter cells were developed as previously described.[21] Only cells within 10–25 passages were used. First, Ibidi 8-well chamber slides (Fitchburg, WI) were coated with poly-D lysine (Thermo Fisher, Federal Way, WA) and rinsed three times with PBS prior to reporter cell seeding at 60,000 cells per well in complete media. After allowing reporter cells to adhere overnight, LNPs or PFV-LNPs were diluted in PBS and added dropwise onto the media for a final concentration of 50 ng or 200 ng mRNA per well and incubated for 24 hours. Following incubation, the media from each well was gently aspirated, and reporter cells were carefully rinsed twice with PBS and fixed with 4% paraformaldehyde diluted in PBS for 10 minutes at room temperature. Upon fixing, wells were gently washed twice more with PBS to remove excess 4% paraformaldehyde. 4′,6-diamidino-2-phenylindole (DAPI) (Thermo Fisher, Federal Way, WA) was then diluted at 1:1000 in PBS and added to each well for nuclear staining. Reporter cells were then washed twice more and mounted with a coverslip using ProLong Diamond Antifade for the mountant (Thermo Fisher, Federal Way, WA). A confocal microscope Leica DMi8 (Leica Microsystems) was used to visualize GFP-positive puncta under a 40x oil immersion objective.

Quantification of Gal9-GFP puncta was performed using ImageJ software, where confocal image z-stacks were preprocessed using maximum intensity projection and a radius of 1 for Gaussian smoothing. The Find Maxima function with a prominence of 75 was used for GFP+ puncta counting. Nuclei counts were collected during analysis with standard segmentation procedures (automatic thresholding and watershed), and normalized recruitment of Galectin-9 was reported as the number of GFP puncta divided by the number of cells.

Intravenous injections and *in vivo* imaging

Female BALB/c mice aged 5–8 weeks were administered 1.5 μg (or 0.06 mg/kg dose) of standard LNPs or PFV-LNP encapsulating FLuc mRNA intravenously via retroorbital injection. At 4-hour and 24-hour time points post-injection, mice were anesthetized with isoflurane and injected with 150 mg of D-luciferin/kg body weight intraperitoneally according to the manufacturer's protocol (Gold Biotechnology, Olivette, MO). Bioluminescent imaging was conducted on IVIS Lumina XRMS (PerkinElmer, Waltham, MA) and image analysis was performed in Living Image Software (PerkinElmer, Waltham, MA).

Subretinal administration

Prior to subretinal injections, mice were topically administered 0.5% proparacaine, 1% tropicamide, and 2.5% phenylephrine and anesthetized with ketamine (100 mg/kg)/xylazine

(10 mg/kg). To initiate the injection, 2.5% hypromellose was placed over the eye and a 30-gauge needle was used to make an incision in the limbus. A glass coverslip was then placed over the eye to allow for visualization of the retina. Going through the incision in the limbus, 1 μL of PBS or LNP material was delivered to the subretinal space via a Hamilton syringe with a 33-gauge blunt needle. Each mouse received LNP or PFV-LNP treatment in one eye and PBS (control) in the contralateral eye. A 2% fluorescein solution was added to the treatment solutions so retinal detachment could be easily observed and documented. For most injections, incisions in the limbus were created nasally and PBS or LNPs were delivered temporally.

Fundus photography in mice

Live, *in-vivo* retinal imaging was performed with the Micron IV (Phoenix Research Laboratories, Pleasanton, CA). Bright-field images were acquired to observe general retinal health. A 534/42 nm BrightLine® single-band bandpass filter (Semrock, Rochester, NY) was used to capture tdTomato signal, and a 475/534 nm BrightLine® filter was used for EGFP imaging. Light intensity, exposure and gain were kept consistent across all RFP and GFP images. ImageJ software (National Institutes of Health, Bethesda, MD) was used to compare reporter expression across fundus images.

Immunofluorescence (IF) sample preparation

Mice were sacrificed immediately after fundus imaging, and a superior corneal burn mark was made to ensure proper orientation following whole globe enucleation. Harvested eyes were immediately placed in 4% paraformaldehyde (PFA) and designated for cryosectioning or flatmounting.

For cryosection imaging (Cre recombinase and EGFP), whole globes were incubated in 4% PFA overnight at 4 °C. The next day, whole globes were incubated in 30% sucrose in PBS for 2 hours at 4 °C before embedding in cryostat compound (Tissue-Tek O.C.T. Compound, code # 4583). The embedded eyes were snap-frozen in a dry ice bath. Eyes were sectioned at 12 μm on a cryostat (Microtome HM550; Walldorf, Germany). Samples were stored at −20 °C until staining. Frozen cryosections were incubated at room temperature for at least 30 minutes and rehydrated in 1X PBS. Sections from 129X1/SvJ mice were permeabilized and blocked for 1 hour in a 1% bovine serum albumin (BSA)/0.3% Triton mixture and were treated with an anti-GFP antibody (1:500, chicken, ab13970) diluted in the same mixture overnight at 4 °C. Sections were washed the following day with PBS and incubated in a secondary antibody (goat anti-chicken Alexa 488, 1:500, Cat#A11039) for 1 hour at room temperature and counter-stained with DAPI for 5 minutes in the dark at room temperature. Sections from Ai9 mice were rehydrated and washed with 1X PBS and similarly counter-stained with DAPI. After a final rinse, retinal sections were mounted in a Fluoromount-G, and cover-slipped.

Eyes designated for flatmount imaging were fixed in 4% PFA for 30 minutes at 4°C in the dark, then incubated in sucrose overnight at 4°C in the dark, and dissected according to a previously published protocol.[46] Leica M60 microscope was used for flatmount dissections. During dissection, the cornea was cut off, the superior side of the eye cup was marked by

cutting a triangular notch at the burn mark, and the whole neural retina was removed before making 4 symmetrical radial cuts in the remaining eye cup to the optic nerve head. RPE was placed on a labeled slide with the superior petal at the top of the slide. Immunostaining with a ZO-1 polyclonal rabbit primary antibody at a dilution of 1:50 (Invitrogen, 61–7300) was performed on the RPE flatmounts using a 0.5% BSA/2.5% donkey serum blocking buffer overnight at 4°C in the dark. The next day, sections were washed with PBS and incubated in an Alexa Fluor™ Plus 488 goat anti-rabbit secondary antibody at a dilution of 1:800 (Invitrogen, A32731), and DAPI (0.5 μg/mL) for 2 hours at room temperature in the dark. After immunostaining, RPE flatmounts were mounted on Prolong Diamond mounting media (Invitrogen, P36961) and coverslipped.

Murine retina imaging and EGFP image analysis

Retinal sections were analyzed by the TCS SP8 X (Leica Microsystems, Buffalo Grove, IL) confocal microscope. All the images were captured with identical exposure settings at 40x magnification using Z-stacks. Z-stacks (spanned 10 μm with 1 μm interval) were collected using a 40X objective, and maximum intensity projections were reported. IF images were analyzed for fluorescence intensity using ImageJ.

For quantification of GFP fluorescence in fundus and IF images, the region of interest was selected and pixel intensity was quantified in ImageJ (version 1.53t; National Institutes of Health, Bethesda, MD). Average pixel intensity of the ROI was calculated along the Mean Gray Scale (%) where 0% indicates black pixels and 100% indicates white pixels, and this intensity measurement was reported as a Mean Gray Value (MGV). All fundus and IF images of PBS injected control eyes were converted to 16-bit grayscale to calculate background MGVs used to establish a threshold for GFP expression. The entire retinal area of fundus control images was included when obtaining these background MGVs. For IF images, the background MGV measurements were taken by adjusting the selection of the control images to include only the retinal tissue. Then, the MGVs of GFP expression for all LNP-injected fundus and IF images were calculated by setting the threshold to only calculate the MGV using intensity values above the background MGVs previously established from the corresponding PBS control images.

Quantification of gene editing

To calculate the editing events in the RPE flatmounts, images across the entire RPE flatmounts were taken at 10x magnification and stitched together using a Keyence BZ-X710 All-in-One Fluorescence scanning Microscope. The total flatmount area was defined using the polygon selections tool, subtracting the area for the optical nerve head. To identify the area of the injection site, the regions of tdTomato expression within the flatmount RPE were initially traced by automatic Otsu thresholding in the tdTomato channel, and corrected manually using the polygon selections tool. Then, the expression of tdTomato was measured as the total area of tdTomato+ pixels within the treated area or the total flatmount area. To assess the damage, RPE was stained with a ZO-1 membrane stain. Regions with disrupted cell membrane morphology within the injection site were considered damaged, and their area was measured using the polygon tool. The total percent of intact cells was reported as a percentage of the intact area within the injection site relative to the total area of the treated

bleb or to the total flatmount. An unpaired t-test in GraphPad Prism was used to calculate statistics. Quantification of gene editing via next-gen sequencing (NGS) was performed identically to our previously published work.[39]

NHP in vivo delivery and imaging

On the day of surgery, pupils were dilated to a minimum of 8 mm using phenylephrine (2.5%; Bausch and Lomb, Rochester, NY, USA) and tropicamide (1% tropicacyl; Akorn, Lake Forest, IL, USA) eye drops. PFV-LNPs were administered into the subretinal space through a 27G/38G subretinal cannula (#5194, Microvision, Redmond, WA, USA) using an Alcon Constellation vitrectomy machine and a pars plana transvitreal approach. A 50 µl subretinal bleb was generated with either saline as control or PFV-LNPs at 500 ng/µl EGFP mRNA. After the injection, dexamethasone (0.5 ml and 10 mg/ml) and cefazolin (0.5 ml and 125 mg/ml) were administered subconjunctivally. There were no complications noted during surgery. The animal received comprehensive multimodal retinal imaging before injection (baseline) and at 48 hours after injection. For each imaging session, the animal was anesthetized by an intramuscular injection of Telazol (1:1 mixture of tiletamine hydrochloride and zolazepam hydrochloride, 3.5 to 5.0 mg/kg) and maintained with ketamine (1 to 2 mg/kg) as required. Heart rate and peripheral blood oxygen saturation were monitored by pulse oximetry. Rectal temperature was maintained between 37.0° and 38.0°C by water-circulating heated pads. For image acquisition, the animal was positioned prone with the head supported by a chinrest; the pupils were dilated to a minimum of 8 mm using phenylephrine (2.5%; Bausch and Lomb, Rochester, NY, USA) and tropicamide (1% tropicacyl; Akorn, Lake Forest, IL, USA) eye drops. A speculum was inserted to hold the lids open, and custom contact lenses were placed on the cornea to maintain hydration and improve image quality. Imaging included fundus autofluorescence and SD-OCT (Spectralis, Heidelberg, Franklin, MA). Following imaging, contact lenses and eyelid specula were removed, and erythromycin ointment was applied to each eye.

NHP immunofluorescence imaging

Following humane euthanasia by a veterinary pathologist, eyes were collected and immersion fixed in 4% paraformaldehyde in PBS for 24 hours. Fixed eye cups were cryoprotected in 10%, 20% and 30% sucrose solutions, embedded in OCT compound, and sectioned using a Leica cryostat (CM1850, Leica, Wetzlar, Germany) at 16µm. Every slide was visualized for native GFP expression to identify the borders of each bleb. For quantification of LNP expression, primary antibodies consisted of anti-GFP (ab290, Abcam, Cambridge, UK), anti-cone arrestin, and anti-rod arrestin (generously provided by W.C. Smith at UF). Secondaries included a combination of Alexa Fluor 488 (GFP), Alex Fluor 568 (rods) and Alexa Fluor 633 (cones), which were used at 1:300 dilution. All slides were counterstained with DAPI.

NHP Photoreceptor quantification

10 representative 20x confocal microscope images were collected with uniform laser intensity settings for EGFP, cone arrestin, and RPE fluorescence. For each image, total cone, total rod, total RPE, and GFP+ cone, rod, and RPE counts were generated by manual

counting. The GFP+ cell counts were divided by the respective total cell counts to generate a % transfected cones and % transfected rods, respectively.

Generation of human retinal organoids

The human iPSCs used in this study were generated from healthy control patient blood samples, which were collected after informed consent. This work was approved by the Institutional Review Board (IRB# 2735) at Oregon Health & Science University. Retinal organoids were generated using a previously published protocol.[53] Briefly, human induced pluripotent stem cells (iPSCs) were grown on Corning® Matrigel® Basement Membrane Matrix-coated plates (354234 - Corning®, Corning, NY) in mTeSR Plus medium, which was exchanged every other day. To start differentiating the iPSCs, cells were rinsed with 1x Dulbecco's phosphate-buffered saline (DPBS) before applying EDTA (1:1000 in 1x DPBS) to the cells for 2–3 minutes. EDTA was then aspirated and cells were given fresh mTeSR Plus medium before colonies were gently lifted using a cell lifter. Colonies used to make retinal organoids were carried through the differentiation protocol as previously described. Phase images of the retinal organoids were captured using a Leica DMI3000B inverted microscope.

Human organoid transfection and immunolabeling

Retinal organoids were grown for 240–400 days in culture using a previously described procedure.[53] 30 min prior to transfection, organoids (and any associated RPE clusters) were transferred to a 96-well tissue culture-treated U-bottom plate (Corning, 3799) in Opti-MEM medium (ThermoFisher, 31985062). To transfect the organoids or RPE cells, the OptiMEM media was removed from each well and the appropriate volume of LNPs (to achieve 2μg, 5μg, 10μg, or 15μg of mRNA) or PBS (negative control) was slowly applied directly on top of the organoids. After incubating the organoids with LNPs at room temperature for 10 minutes, 100μL of OptiMEM was slowly applied to each well, and the organoids were returned to the 37°C incubator. At 4 hours post-transfection, 100μL of retinal organoid medium (3D-RDM) was applied to each well.

To analyze transfection output, retinal organoids were collected at 48 hours post-transfection and fixed for 30 minutes in 4% paraformaldehyde. Tissue cryosections were stained with anti-GFP (1:100, Abcam ab13970) or anti-green/red cone opsin (G/RCO; 1:100, gift from Jeremy Nathans Lab) antibodies. Nuclei were counterstained with 4′,6-diamidino-2-phenylindole (DAPI, 1 μg/mL; Roche, 10236276001) for 3 minutes, and the sections were imaged on a Leica SP8 confocal microscope.

Statistical Analysis

The data were analyzed using GraphPad Prism and expressed as a mean ± standard deviation (mean ± SD). Unless stated otherwise, statistical analysis was performed via one-way or two-way analysis of variance (ANOVA) tests with post hoc Tukey's multiple comparison test. P-values less than 0.05 were considered statistically significant (*$p \leq 0.05$, **$p \leq 0.01$, ***$p \leq 0.001$, ****$p \leq 0.0001$). Values $p > 0.05$ were considered not statistically significant (ns). Where applicable, outliers were removed via ROUT method (Q=1%). For characterization and in vitro assays, data were collected with at least 3 technical replicates

and reproduced in at least three different experiment sets. In vivo data in mice for EGFP and Cre recombinase mRNA were collected from 3–4 independent study samples (3 mice per group in intravenous injection studies or 4 eyes per group in subretinal injection studies), with EGFP analysis for MC3 LNPs and PFV-LNPs reproduced twice. Flatmount and NGS analysis were performed with n=7–9 eyes each. Non-human primate and retinal organoid data used N=1 replicates.

Supplementary Material

Refer to Web version on PubMed Central for supplementary material.

Acknowledgements

We would like to thank the Casey Eye Institute (CEI) Leonard Christenson Eye Pathology Laboratory and Oregon National Primate Research Center (ONPRC) for their support with experiments, tissue processing, and sectioning. Electron microscopy was performed at the Multiscale Microscopy Core (MMC), a member of the OHSU University Shared Resource Cores; some acquisition was performed with technical support from Steven Adamou. Some illustrations were created with BioRender.com.

Funding

This project was supported through funding from the National Eye Institute 1R01EY033423-01A1 (G.S.), ONPRC Pilot Grant (R.C.R.), ONPRC Core Grant P51 OD011092 and S10RR024585, CEI Core Grant P30 EY010572 from the National Institutes of Health, unrestricted departmental funding from Research to Prevent Blindness, and the Malcolm M. Marquis, MD Endowed Fund for Innovation.

Bibliography

(1). Boye SE; Boye SL; Lewin AS; Hauswirth WW A Comprehensive Review of Retinal Gene Therapy. Mol. Ther. 2013, 21 (3), 509–519. 10.1038/mt.2012.280. [PubMed: 23358189]

(2). Russell S; Bennett J; Wellman JA; Chung DC; Yu Z-F; Tillman A; Wittes J; Pappas J; Elci O; McCague S; Cross D; Marshall KA; Walshire J; Kehoe TL; Reichert H; Davis M; Raffini L; George LA; Hudson FP; Dingfield L; Zhu X; Haller JA; Sohn EH; Mahajan VB; Pfeifer W; Weckmann M; Johnson C; Gewaily D; Drack A; Stone E; Wachtel K; Simonelli F; Leroy BP; Wright JF; High KA; Maguire AM Efficacy and Safety of Voretigene Neparvovec (AAV2-hRPE65v2) in Patients with RPE65-Mediated Inherited Retinal Dystrophy: A Randomised, Controlled, Open-Label, Phase 3 Trial. The Lancet 2017, 390 (10097), 849–860. 10.1016/S0140-6736(17)31868-8.

(3). Kim J; Eygeris Y; Ryals RC; Jozić A; Sahay G Strategies for Non-Viral Vectors Targeting Organs beyond the Liver. Nat. Nanotechnol. 2023, 1–20. 10.1038/s41565-023-01563-4. [PubMed: 36418490]

(4). Hajj KA; Whitehead KA Tools for Translation: Non-Viral Materials for Therapeutic mRNA Delivery. Nat. Rev. Mater. 2017, 2 (10), 17056. 10.1038/natrevmats.2017.56.

(5). Zulliger R; Conley SM; Naash MI Non-Viral Therapeutic Approaches to Ocular Diseases: An Overview and Future Directions. J. Control. Release Off. J. Control. Release Soc 2015, 219, 471–487. 10.1016/j.jconrel.2015.10.007.

(6). Kristen AV; Ajroud-Driss S; Conceição I; Gorevic P; Kyriakides T; Obici L Patisiran, an RNAi Therapeutic for the Treatment of Hereditary Transthyretin-Mediated Amyloidosis. Neurodegener. Dis. Manag. 2019, 9 (1), 5–23. 10.2217/nmt-2018-0033. [PubMed: 30480471]

(7). Camaschella C Treating Iron Overload. N. Engl. J. Med. 2013, 368 (24), 2325–2327. 10.1056/NEJMcibr1304338. [PubMed: 23758239]

(8). Alberer M; Gnad-Vogt U; Hong HS; Mehr KT; Backert L; Finak G; Gottardo R; Bica MA; Garofano A; Koch SD; Fotin-Mleczek M; Hoerr I; Clemens R; von Sonnenburg F Safety and Immunogenicity of a mRNA Rabies Vaccine in Healthy Adults: An Open-Label, Non-

Randomised, Prospective, First-in-Human Phase 1 Clinical Trial. Lancet Lond. Engl. 2017, 390 (10101), 1511–1520. 10.1016/S0140-6736(17)31665-3.

(9). Polack FP; Thomas SJ; Kitchin N; Absalon J; Gurtman A; Lockhart S; Perez JL; Pérez Marc G; Moreira ED; Zerbini C; Bailey R; Swanson KA; Roychoudhury S; Koury K; Li P; Kalina WV; Cooper D; Frenck RW; Hammitt LL; Türeci Ö; Nell H; Schaefer A; Ünal S; Tresnan DB; Mather S; Dormitzer PR; Şahin U; Jansen KU; Gruber WC Safety and Efficacy of the BNT162b2 mRNA Covid-19 Vaccine. N. Engl. J. Med. 2020, 383 (27), 2603–2615. 10.1056/NEJMoa2034577. [PubMed: 33301246]

(10). Baden LR; El Sahly HM; Essink B; Kotloff K; Frey S; Novak R; Diemert D; Spector SA; Rouphael N; Creech CB; McGettigan J; Khetan S; Segall N; Solis J; Brosz A; Fierro C; Schwartz H; Neuzil K; Corey L; Gilbert P; Janes H; Follmann D; Marovich M; Mascola J; Polakowski L; Ledgerwood J; Graham BS; Bennett H; Pajon R; Knightly C; Leav B; Deng W; Zhou H; Han S; Ivarsson M; Miller J; Zaks T Efficacy and Safety of the mRNA-1273 SARS-CoV-2 Vaccine. N. Engl. J. Med. 2021, 384 (5), 403–416. 10.1056/NEJMoa2035389. [PubMed: 33378609]

(11). Gillmore JD; Gane E; Taubel J; Kao J; Fontana M; Maitland ML; Seitzer J; O'Connell D; Walsh KR; Wood K; Phillips J; Xu Y; Amaral A; Boyd AP; Cehelsky JE; McKee MD; Schiermeier A; Harari O; Murphy A; Kyratsous CA; Zambrowicz B; Soltys R; Gutstein DE; Leonard J; Sepp-Lorenzino L; Lebwohl D CRISPR-Cas9 In Vivo Gene Editing for Transthyretin Amyloidosis. N. Engl. J. Med. 2021, 385 (6), 493–502. 10.1056/NEJMoa2107454. [PubMed: 34215024]

(12). Eygeris Y; Gupta M; Kim J; Sahay G Chemistry of Lipid Nanoparticles for RNA Delivery. Acc. Chem. Res. 2022, 55 (1), 2–12. 10.1021/acs.accounts.1c00544. [PubMed: 34850635]

(13). Granot Y; Peer D Delivering the Right Message: Challenges and Opportunities in Lipid Nanoparticles-Mediated Modified mRNA Therapeutics—An Innate Immune System Standpoint. Semin. Immunol. 2017, 34, 68–77. 10.1016/j.smim.2017.08.015. [PubMed: 28890238]

(14). Hou X; Zaks T; Langer R; Dong Y Lipid Nanoparticles for mRNA Delivery. Nat. Rev. Mater. 2021, 1–17. 10.1038/s41578-021-00358-0.

(15). Hassett KJ; Higgins J; Woods A; Levy B; Xia Y; Hsiao CJ; Acosta E; Almarsson Ö; Moore MJ; Brito LA Impact of Lipid Nanoparticle Size on mRNA Vaccine Immunogenicity. J. Controlled Release 2021. 10.1016/J.JCONREL.2021.05.021.

(16). Kulkarni JA; Thomson SB; Zaifman J; Leung J; Wagner PK; Hill A; Tam YYC; Cullis PR; Petkau TL; Leavitt BR Spontaneous, Solvent-Free Entrapment of siRNA within Lipid Nanoparticles. Nanoscale 2020, 12 (47), 23959–23966. 10.1039/d0nr06816k. [PubMed: 33241838]

(17). Leppek K; Byeon GW; Kladwang W; Wayment-Steele HK; Kerr CH; Xu AF; Kim DS; Topkar VV; Choe C; Rothschild D; Tiu GC; Wellington-Oguri R; Fujii K; Sharma E; Watkins AM; Nicol JJ; Romano J; Tunguz B; Diaz F; Cai H; Guo P; Wu J; Meng F; Shi S; Participants E; Dormitzer PR; Solórzano A; Barna M; Das R Combinatorial Optimization of mRNA Structure, Stability, and Translation for RNA-Based Therapeutics. Nat. Commun. 2022, 13 (1), 1536. 10.1038/s41467-022-28776-w. [PubMed: 35318324]

(18). Blakney AK; McKay PF; Yus BI; Aldon Y; Shattock RJ Inside out: Optimization of Lipid Nanoparticle Formulations for Exterior Complexation and in Vivo Delivery of saRNA. Gene Ther. 2019, 26 (9), 363–372. 10.1038/s41434-019-0095-2. [PubMed: 31300730]

(19). Leung AKK; Tam YYC; Chen S; Hafez IM; Cullis PR Microfluidic Mixing: A General Method for Encapsulating Macromolecules in Lipid Nanoparticle Systems. J. Phys. Chem. B 2015, 119 (28), 8698–8706. 10.1021/acs.jpcb.5b02891. [PubMed: 26087393]

(20). Sanchez SA; Tricerri MA; Gratton E Laurdan Generalized Polarization Fluctuations Measures Membrane Packing Micro-Heterogeneity in Vivo. Proc. Natl. Acad. Sci. 2012, 109 (19), 7314–7319. 10.1073/pnas.1118288109. [PubMed: 22529342]

(21). Henderson MI; Eygeris Y; Jozic A; Herrera M; Sahay G Leveraging Biological Buffers for Efficient Messenger RNA Delivery via Lipid Nanoparticles. Mol. Pharm. 2022, 19 (11), 4275–4285. 10.1021/acs.molpharmaceut.2c00587. [PubMed: 36129254]

(22). Koitabashi K; Nagumo H; Nakao M; Machida T; Yoshida K; Sakai-Kato K Acidic pH-Induced Changes in Lipid Nanoparticle Membrane Packing. Biochim. Biophys. Acta BBA - Biomembr. 2021, 1863 (8), 183627. 10.1016/j.bbamem.2021.183627.

(23). Jayaraman M; Ansell SM; Mui BL; Tam YK; Chen J; Du X; Butler D; Eltepu L; Matsuda S; Narayanannair JK; Rajeev KG; Hafez IM; Akinc A; Maier MA; Tracy MA; Cullis PR; Madden TD; Manoharan M; Hope MJ Maximizing the Potency of siRNA Lipid Nanoparticles for Hepatic Gene Silencing In Vivo. Angew. Chem. Int. Ed. 2012, 51 (34), 8529–8533. 10.1002/anie.201203263.

(24). Eygeris Y; Patel S; Jozic A; Sahay G Deconvoluting Lipid Nanoparticle Structure for Messenger RNA Delivery. Nano Lett. 2020, 20 (6), 4543–4549. 10.1021/acs.nanolett.0c01386. [PubMed: 32375002]

(25). Cheng MHY; Leung J; Zhang Y; Strong C; Basha G; Momeni A; Chen Y; Jan E; Abdolahzadeh A; Wang X; Kulkarni JA; Witzigmann D; Cullis PR Induction of Bleb Structures in Lipid Nanoparticle Formulations of mRNA Leads to Improved Transfection Potency. Adv. Mater. 2023, 35 (31), 2303370. 10.1002/adma.202303370.

(26). Kulkarni JA; Witzigmann D; Leung J; Tam YYC; Cullis PR On the Role of Helper Lipids in Lipid Nanoparticle Formulations of siRNA. Nanoscale 2019, 11 (45), 21733–21739. 10.1039/C9NR09347H. [PubMed: 31713568]

(27). Yanez Arteta M; Kjellman T; Bartesaghi S; Wallin S; Wu X; Kvist AJ; Dabkowska A; Székely N; Radulescu A; Bergenholtz J; Lindfors L Successful Reprogramming of Cellular Protein Production through mRNA Delivered by Functionalized Lipid Nanoparticles. Proc. Natl. Acad. Sci. 2018, 115 (15), E3351–E3360. 10.1073/pnas.1720542115. [PubMed: 29588418]

(28). Ramezanpour M; Tieleman DP Computational Insights into the Role of Cholesterol in Inverted Hexagonal Phase Stabilization and Endosomal Drug Release. Langmuir 2022, 38 (24), 7462–7471. 10.1021/acs.langmuir.2c00430. [PubMed: 35675506]

(29). Larson NR; Hu G; Wei Y; Tuesca AD; Forrest ML; Middaugh CR pH-Dependent Phase Behavior and Stability of Cationic Lipid–mRNA Nanoparticles. J. Pharm. Sci. 2022, 111 (3), 690–698. 10.1016/j.xphs.2021.11.004. [PubMed: 34774918]

(30). Heyes J; Palmer L; Bremner K; MacLachlan I Cationic Lipid Saturation Influences Intracellular Delivery of Encapsulated Nucleic Acids. J. Controlled Release 2005, 107 (2), 276–287. 10.1016/J.JCONREL.2005.06.014.

(31). Cullis PR; Hope MJ Lipid Nanoparticle Systems for Enabling Gene Therapies. Mol. Ther. 2017, 25 (7), 1467–1475. 10.1016/J.YMTHE.2017.03.013. [PubMed: 28412170]

(32). Sebastiani F; Yanez Arteta M; Lerche M; Porcar L; Lang C; Bragg RA; Elmore CS; Krishnamurthy VR; Russell RA; Darwish T; Pichler H; Waldie S; Moulin M; Haertlein M; Forsyth VT; Lindfors L; Cárdenas M Apolipoprotein E Binding Drives Structural and Compositional Rearrangement of mRNA-Containing Lipid Nanoparticles. ACS Nano 2021, acsnano.0c10064. 10.1021/acsnano.0c10064.

(33). Patel S; Ashwanikumar N; Robinson E; Xia Y; Mihai C; Griffith JP; Hou S; Esposito AA; Ketova T; Welsher K; Joyal JL; Almarsson Ö; Sahay G Naturally-Occurring Cholesterol Analogues in Lipid Nanoparticles Induce Polymorphic Shape and Enhance Intracellular Delivery of mRNA. Nat. Commun. 2020, 11 (1), 983. 10.1038/s41467-020-14527-2. [PubMed: 32080183]

(34). Herrera M; Kim J; Eygeris Y; Jozic A; Sahay G Illuminating Endosomal Escape of Polymorphic Lipid Nanoparticles That Boost mRNA Delivery. Biomater. Sci. 2020, 2020.12.02.407601. 10.1039/D0BM01947J.

(35). Munson MJ; O'Driscoll G; Silva AM; Lázaro-Ibáñez E; Gallud A; Wilson JT; Collén A; Esbjörner EK; Sabirsh A A High-Throughput Galectin-9 Imaging Assay for Quantifying Nanoparticle Uptake, Endosomal Escape and Functional RNA Delivery. Commun. Biol. 2021, 4 (1), 1–14. 10.1038/s42003-021-01728-8. [PubMed: 33398033]

(36). Ryals RC; Patel S; Acosta C; McKinney M; Pennesi ME; Sahay G The Effects of PEGylation on LNP Based mRNA Delivery to the Eye. PLOS ONE 2020, 15 (10), e0241006. 10.1371/journal.pone.0241006. [PubMed: 33119640]

(37). Patel S; Ryals RC; Weller KK; Pennesi ME; Sahay G Lipid Nanoparticles for Delivery of Messenger RNA to the Back of the Eye. J. Controlled Release 2019, 303, 91–100. 10.1016/j.jconrel.2019.04.015.

(38). Madisen L; Zwingman TA; Sunkin SM; Oh SW; Zariwala HA; Gu H; Ng LL; Palmiter RD; Hawrylycz MJ; Jones AR; Lein ES; Zeng H A Robust and High-Throughput Cre Reporting

and Characterization System for the Whole Mouse Brain. Nat. Neurosci. 2010, 13 (1), 133–140. 10.1038/nn.2467. [PubMed: 20023653]

(39). Gautam M; Jozic A; Su GL-N; Herrera-Barrera M; Curtis A; Arrizabalaga S; Tschetter W; Ryals RC; Sahay G Lipid Nanoparticles with PEG-Variant Surface Modifications Mediate Genome Editing in the Mouse Retina. Nat. Commun. 2023, 14 (1), 6468. 10.1038/s41467-023-42189-3. [PubMed: 37833442]

(40). Kam JH; Weinrich TW; Shinhmar H; Powner MB; Roberts NW; Aboelnour A; Jeffery G Fundamental Differences in Patterns of Retinal Ageing between Primates and Mice. Sci. Rep. 2019, 9 (1), 12574. 10.1038/s41598-019-49121-0. [PubMed: 31467395]

(41). Picaud S; Dalkara D; Marazova K; Goureau O; Roska B; Sahel J-A The Primate Model for Understanding and Restoring Vision. Proc. Natl. Acad. Sci. 2019, 116 (52), 26280–26287. 10.1073/pnas.1902292116. [PubMed: 31871177]

(42). Eygeris Y; Gupta M; Kim J; Jozic A; Gautam M; Renner J; Nelson D; Bloom E; Tuttle A; Stoddard J; Reynaga R; Neuringer M; Lauer AK; Ryals RC; Sahay G Thiophene-Based Lipids for mRNA Delivery to Pulmonary and Retinal Tissues. Proc. Natl. Acad. Sci. 2024, accepted.

(43). Wahle P; Brancati G; Harmel C; He Z; Gut G; del Castillo JS; Xavier da Silveira dos Santos A; Yu Q; Noser P; Fleck JS; Gjeta B; Pavlinić D; Picelli S; Hess M; Schmidt GW; Lummen TTA; Hou Y; Galliker P; Goldblum D; Balogh M; Cowan CS; Scholl HPN; Roska B; Renner M; Pelkmans L; Treutlein B; Camp JG Multimodal Spatiotemporal Phenotyping of Human Retinal Organoid Development. Nat. Biotechnol. 2023, 1–11. 10.1038/s41587-023-01747-2. [PubMed: 36653493]

(44). O'Hara-Wright M; Gonzalez-Cordero A Retinal Organoids: A Window into Human Retinal Development. Dev. Camb. Engl. 2020, 147 (24), dev189746. 10.1242/dev.189746.

(45). Finn JD; Smith AR; Patel MC; Shaw L; Youniss MR; Heteren J. van; Dirstine T; Ciullo C; Lescarbeau R; Seitzer J; Shah RR; Shah A; Ling D; Growe J; Pink M; Rohde E; Wood KM; Salomon WE; Harrington WF; Dombrowski C; Strapps WR; Chang Y; Morrissey DV A Single Administration of CRISPR/Cas9 Lipid Nanoparticles Achieves Robust and Persistent In Vivo Genome Editing. Cell Rep. 2018, 22 (9), 2227–2235. 10.1016/j.celrep.2018.02.014. [PubMed: 29490262]

(46). Boatright JH; Dalal N; Chrenek MA; Gardner C; Ziesel A; Jiang Y; Grossniklaus HE; Nickerson JM Methodologies for Analysis of Patterning in the Mouse RPE Sheet. Mol. Vis. 2015, 21, 40–60. [PubMed: 25593512]

(47). Zhang Y; Sun C; Wang C; Jankovic KE; Dong Y Lipids and Lipid Derivatives for RNA Delivery. Chem. Rev. 2021, acs.chemrev.1c00244. 10.1021/acs.chemrev.1c00244.

(48). Ball RL; Bajaj P; Whitehead KA Achieving Long-Term Stability of Lipid Nanoparticles: Examining the Effect of pH, Temperature, and Lyophilization. Int J Nanomedicine 2017, 12, 305–315. 10.2147/IJN.S123062. [PubMed: 28115848]

(49). Zhao P; Hou X; Yan J; Du S; Xue Y; Li W; Xiang G; Dong Y Long-Term Storage of Lipid-like Nanoparticles for mRNA Delivery. Bioact. Mater. 2020, 5 (2), 358–363. 10.1016/j.bioactmat.2020.03.001. [PubMed: 32206737]

(50). Zheng L; Bandara SR; Tan Z; Leal C Lipid Nanoparticle Topology Regulates Endosomal Escape and Delivery of RNA to the Cytoplasm. Proc. Natl. Acad. Sci. 2023, 120 (27), e2301067120. 10.1073/pnas.2301067120. [PubMed: 37364130]

(51). Brader ML; Williams SJ; Banks JM; Hui WH; Zhou ZH; Jin L Encapsulation State of Messenger RNA inside Lipid Nanoparticles. Biophys. J. 2021. 10.1016/J.BPJ.2021.03.012.

(52). Packer M; Gyawali D; Yerabolu R; Schariter J; White P A Novel Mechanism for the Loss of mRNA Activity in Lipid Nanoparticle Delivery Systems; 2021; p 2021.09.21.461221. 10.1101/2021.09.21.461221.

(53). Chirco KR; Chew S; Moore AT; Duncan JL; Lamba DA Allele-Specific Gene Editing to Rescue Dominant CRX-Associated LCA7 Phenotypes in a Retinal Organoid Model. Stem Cell Rep. 2021, 16 (11), 2690–2702. 10.1016/j.stemcr.2021.09.007.

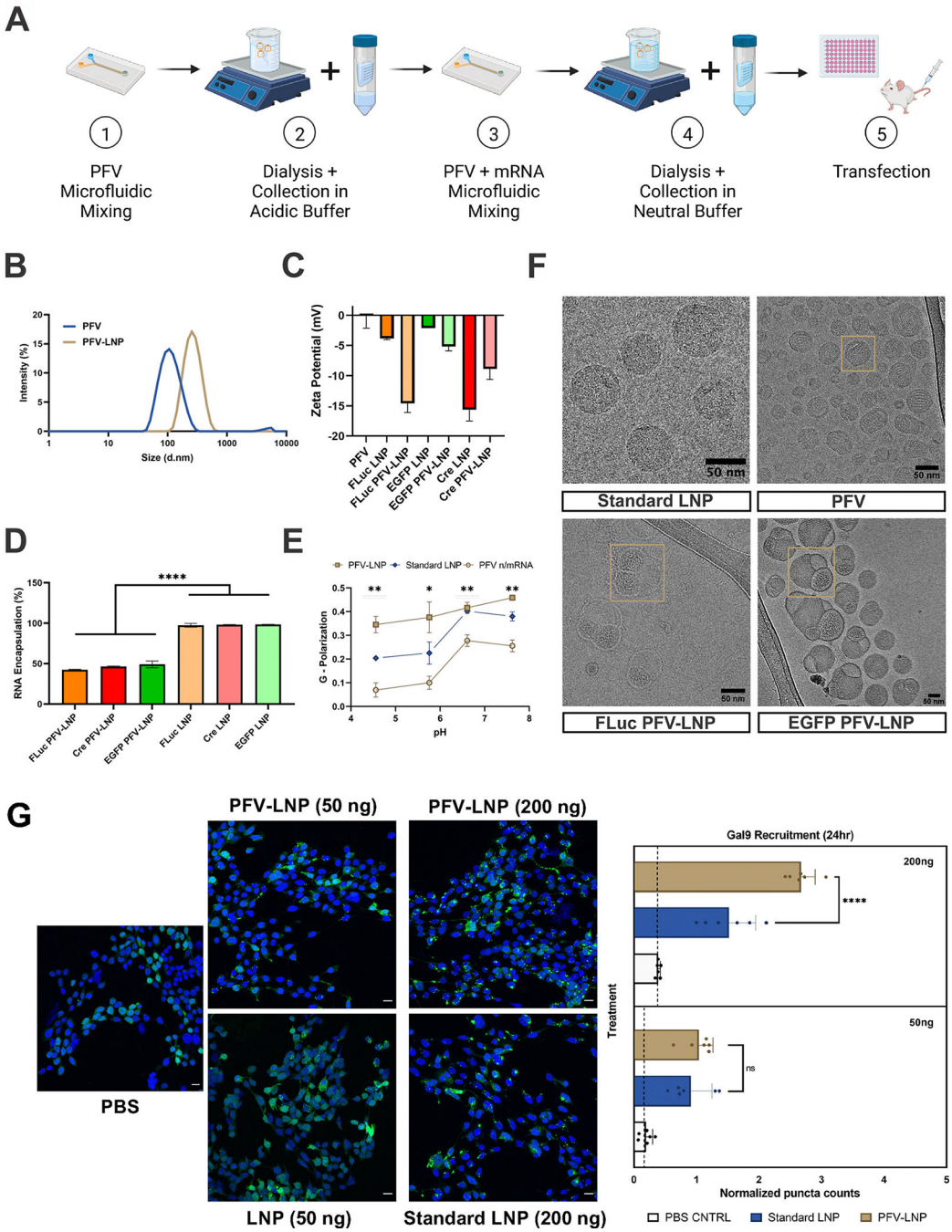

Figure 1. Characterization of lipid nanoparticles (LNP).

(A) Formulation workflow of pre-formed vesicle (PFV) intermediates and mRNA-loaded PFV-LNPs. (B) Representative shift in size distribution for PFV-LNPs compared to unloaded PFV. (C) Zeta potential for PFV, LNP, and PFV-LNP formulations (n=3). (D) Encapsulation efficiency in mRNA-loaded LNPs and PFV-LNPs (n=3). PFV-LNPs consistently have <50% encapsulation efficiency; therefore, the dose is calculated by total mRNA found in sample. (E) Laurdan hydration assay of LNP, PFV, and PFV-LNP formulations, where generalized polarization (GP) is indicative of changes in lipid packing (higher = tighter lipid packing;

n=3). (F) Representative cryo-TEM micrographs of standard LNPs, PFV, or mRNA loaded LNPs with two distinct cargos (FLuc or EGFP mRNA respectively). Gold boxes highlight typical PFV or PFV-LNP morphologies. Scale bars are 50 nm. (G) Gal9 recruitment in modified HEK293T/17 cells treated with LNPs at 24 hours after 50 ng or 200 ng treatment with LNPs. Images presented at maximum intensity projection, DAPI – blue and Gal9-GFP - green. Scale bars represent 50 μm. Quantification includes normalizing Gal9 puncta counts by the number of cells present (from DAPI; n=6). Data are presented as means ± standard deviation. Statistical analyses were performed using ANOVA with Tukey multiple comparison test. n.s.: not significant; *: $p < 0.05$; **: $p < 0.01$; ****: $p < 0.001$. PFV – preformed vesicles approach, no cargo; PFV-LNP – preformed vesicle approach, loaded with mRNA; LNP – standard microfluidic mixing, loaded with mRNA

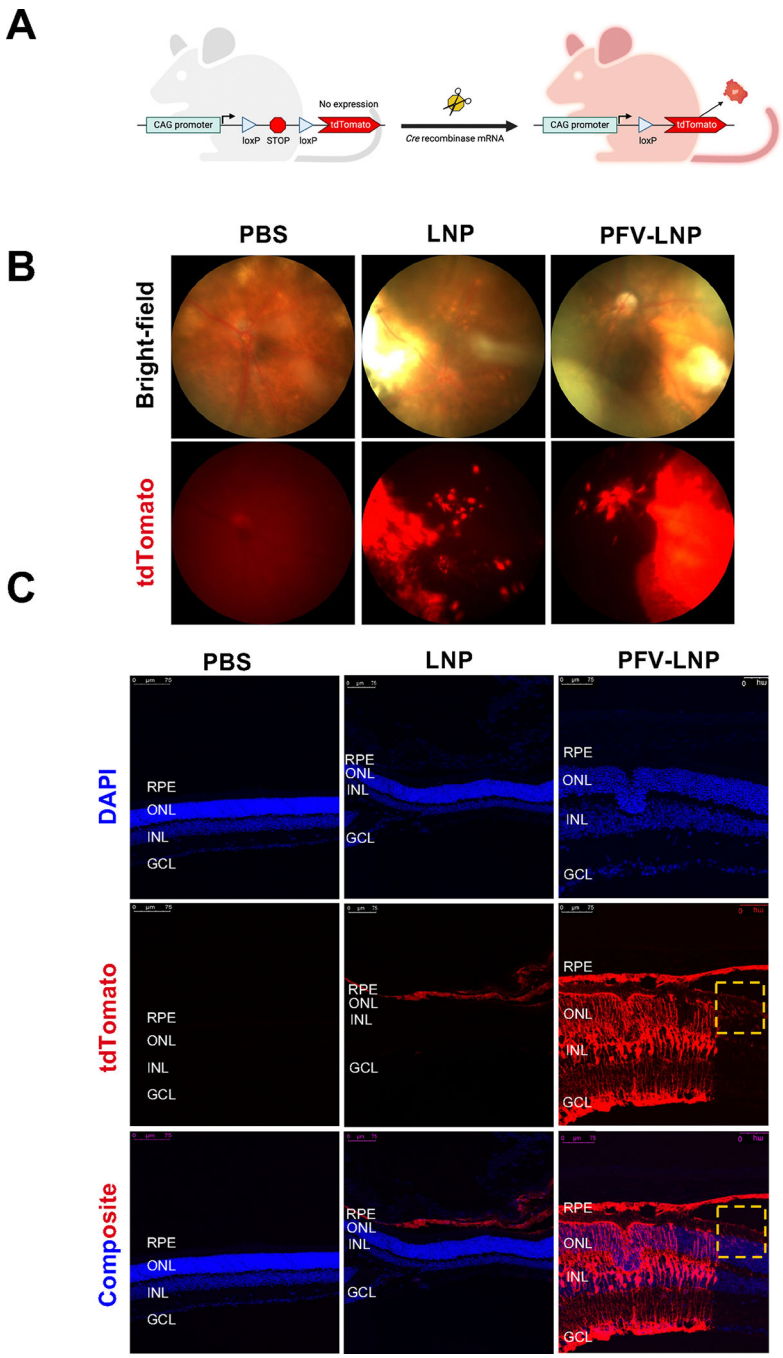

Figure 2. Localization of tdTomato expression after Cre mRNA delivery in Ai9 murine retina.
Nanoparticles were administered via subretinal injection at 400 ng mRNA. Eyes were harvested at the 7-day post-injection and stained with DAPI. (A) Mechanism of Cre-mediated recombination. (B) Representative brightfield (top) and tdTomato (bottom) fundus images for each treatment groups (n=4 eyes each). (C) Representative immunofluorescence images showing tdTomato expression in the RPE and ONL. Gold box indicates the area of photoreceptor transfection. Scale bars represent 75 μm. RPE: retinal pigment epithelium; ONL: outer nuclear layer; INL: inner nuclear layer; GCL: ganglion cell layer.

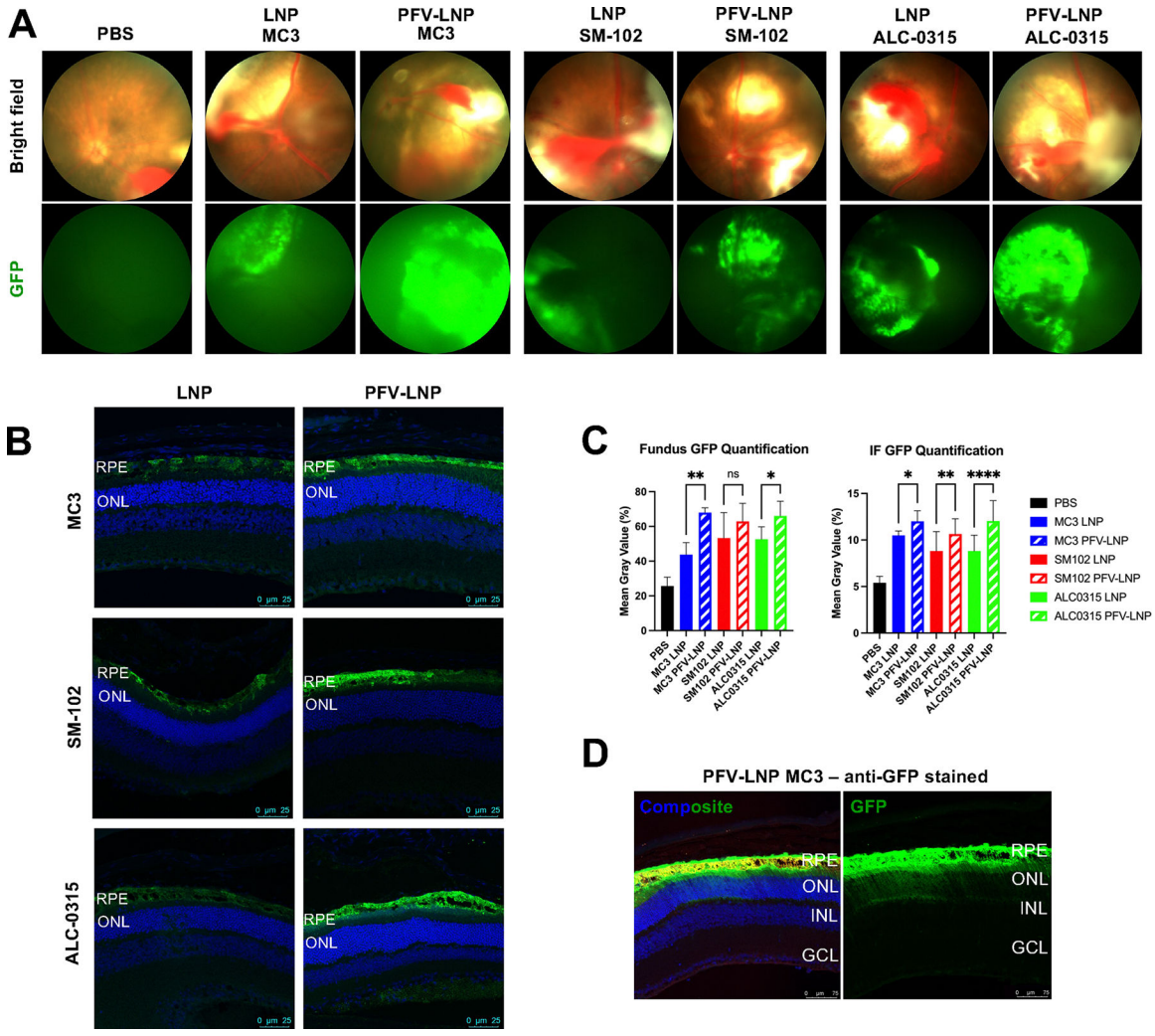

Figure 3. EGFP expression after EGFP mRNA LNP or PFV-LNP treatment in 129X1/SvJ murine retina.

Nanoparticles were administered via subretinal injection at 200 ng mRNA. Eyes were imaged via fundoscopy and harvested at the 48 hours post-injection and processed for IF and imaging. (A) Representative bright field (top) and GFP (bottom) fundus images for each treatment group 48 hours post-injection. (B) Representative immunofluorescence images demonstrate GFP expression in the RPE for LNP groups. (C) Quantification of GFP expression in fundus images (n=4) and in immunofluorescence images (n=4 eyes, with 3–4 individual images per eye). (D) Representative confocal images of IF with showing GFP expression in the RPE and ONL for PFV-LNP group. Data are presented as means ± standard deviation with statistical significance reported using an ordinary one-way ANOVA test. n.s.: not significant; *: $p < 0.05$; **: $p < 0.01$; ****: $p < 0.001$. GFP: green fluorescent protein; RPE: retinal pigment epithelium; ONL: outer nuclear layer; INL: inner nuclear layer; GCL: ganglion cell layer.

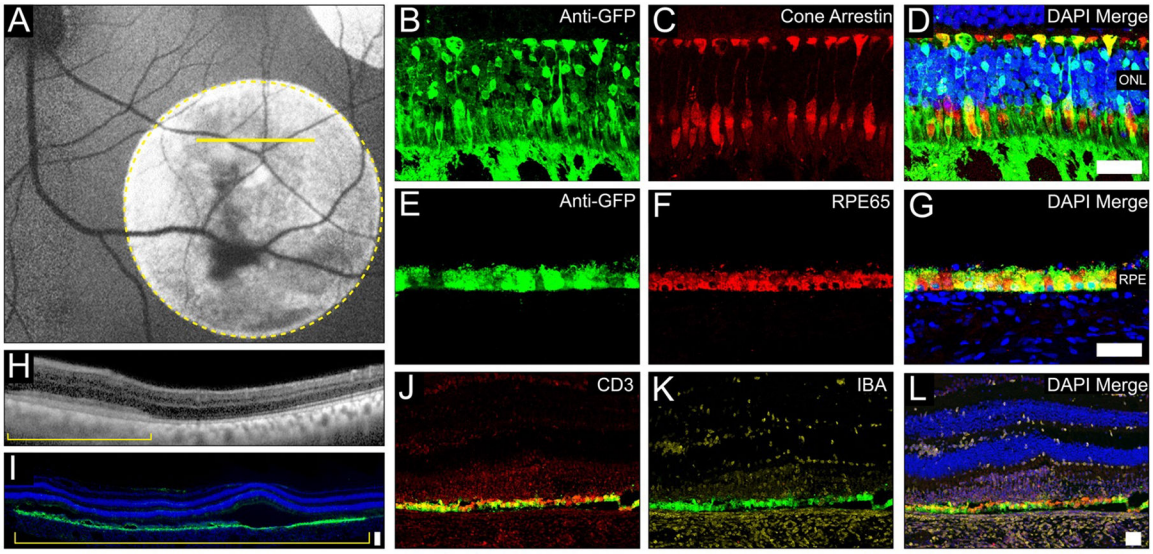

Figure 4. EGFP expression after EGFP mRNA PFV-LNP treatment in non-human primate retina.

Nanoparticles were administered via subretinal injection at 25μg total mRNA dose. NHP eye (N=1) was harvested at the 48 hours post-injection and processed for IF imaging. (A) Representative fundus autofluorescence image 48 hours post-injection indicates prominent EGFP signal (area of the injection bleb highlighted by the dashed circle). (B-D) Representative IF images highlighting transfection in ONL. Transfection of the cone photoreceptors can be confirmed by colocalization of EGFP and cone arrestin signal. (E-G) Representative IF images highlighting transfection in RPE; transfection of RPE can be confirmed by colocalization of EGFP and RPE65 signals. Gross retinal health is visualized by OCT (H; the scanning plane is shown in panel A by yellow line and the bracket demonstrates the area of the injection bleb). (I) DAPI and EGFP composite IF image demonstrates the transfection through the entire injection bleb, with stronger signal observed in RPE. (J-L) Mild immune infiltration through RPE and ONL was observed, as suggested by the CD3 and IBA staining of the retina sections. GFP: green fluorescent protein; RPE: retinal pigment epithelium; ONL: outer nuclear layer.

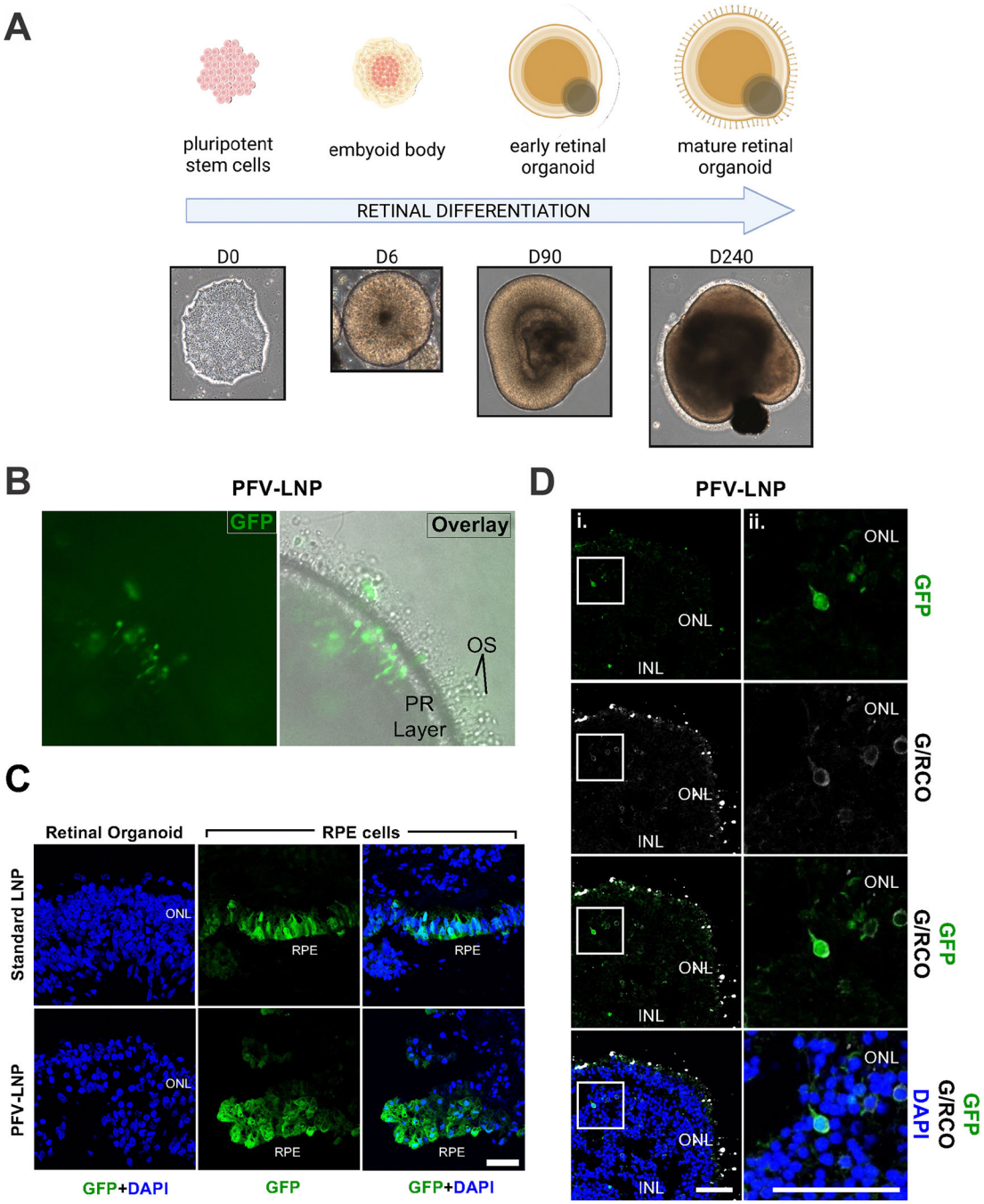

Figure 5. EGFP delivery to human iPSC-derived retinal organoids and RPE cells.

(A) The schematic and brightfield images provide an overview of the differentiation process going from iPSCs to mature retinal organoids. (B) Native EGFP expression (green) is shown in a live control retinal organoid, with and without brightfield overlay, at 48 hours post-PFV-LNP transfection with 2μg *EGFP* mRNA. At 48 hours post-transfection with LNPs or PFV-LNPs carrying *EGFP* mRNA, retinal organoids were fixed, cryosectioned, and immunolabeled. (C) Representative images of organoids or RPE cell clusters after immunolabeling of GFP (green) shows abundant signal in RPE for standard LNPs and

PFV-LNPs. Immunolabeling with antibodies targeting G/RCO (white) shows sparse labeling in cone photoreceptors in retinal organoids (D) transfected with 10μg *EGFP* mRNA in PFV-LNPs. Nuclei are counterstained with DAPI (blue). Panel ii. is the magnified area highlighted in Panel i. GFP: green fluorescent protein; OS: outer segment; PR: photoreceptor; RPE: retinal pigment epithelium; ONL: outer nuclear layer; INL: inner nuclear layer; G/RCO: green/red cone opsin. Scale bars = 50μm.

A

Treatment	EE, %	Size, nm (PDI)	ZP, mV (mean ± std. dev.)
PFV LNP **sgAi9**+Cas9	97.9	89.0 (0.091)	-15.2 ± 2.0
PFV LNP **sgGFP**+Cas9	98.1	93.2 (0.146)	-23.7 ± 2.0
LNP **sgAi9**+Cas9	98.2	122.8 (0.247)	-9.58 ± 2.1
LNP **sgGFP**+Cas9	97.6	94.2 (0.096)	-11.2 ± 2.1

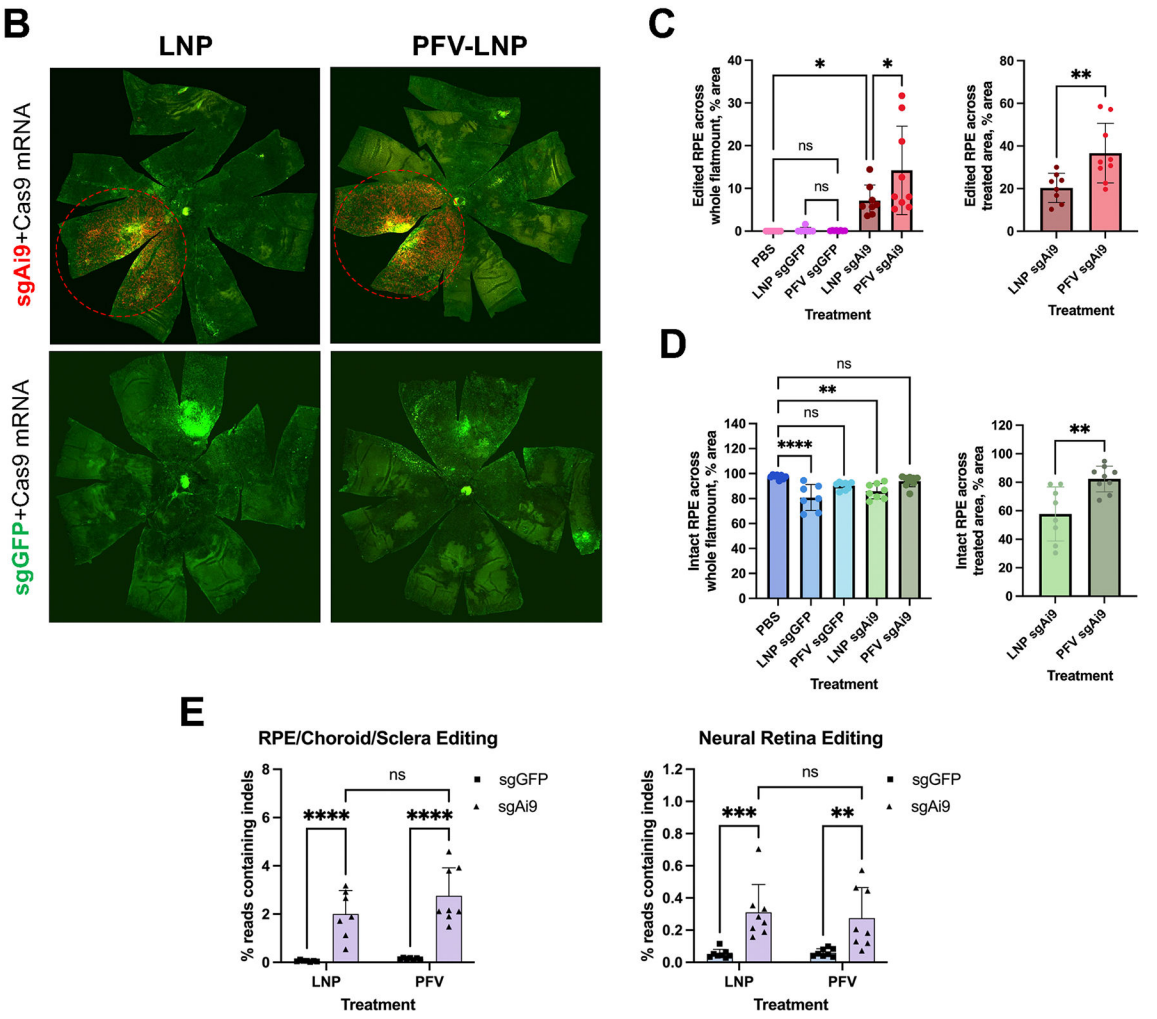

Figure 6. Comparison of gene editing outcomes after PFV-LNP and LNP treatments in Ai9 mice.

(A) Comparison of LP01 PFV-LNP and LNP nanoparticle characteristics. LNPs were administered subretinally at 200 ng total nucleic acid (1:1 wt/wt Cas9 mRNA:sgRNA) and the eyes were harvested 7 days after injection for flatmount and NGS analysis; n = 7–9 in each group. (B) Representative RPE flatmount images (green: ZO-1 staining, red: tdTomato; background removed for visual clarity). Dashed red circles indicate the transfected area. Image-based quantification of gene editing efficiency (C) and retinal health (D) was performed within whole RPE flatmounts and the injection site and presented as % of area. (E) Next-generation sequencing results; some outliers were removed via

ROUT method (Q=1%). No outliers were noted in image-based analysis. Data are presented as means ± standard deviation. Statistical significance reported using ANOVA for image analysis of the whole flatmounts and NGS data, and Welch's t-test for image analysis within the treated areas. n.s.: not significant; *: $p < 0.05$; **: $p < 0.01$; ****: $p < 0.001$. RPE: retinal pigment epithelium, EE: encapsulation efficiency, PDI: polydispersity index, ZP: zeta potential, RPE: retinal pigment epithelium, sgGFP: non-targeting sgRNA, sgAi9: targeting sgRNA.